ACS APPLIED NANO MATERIALS

www.acsanm.org Article

Trimetallic Nanostructures of Silver−Platinum Alloy Shells on Gold Nanorods for Plasmon-Mediated Photocatalysis

Qi Zhang, Tian-Song Deng,* Yun-Qi Dou, Ming-Zhang Wei, Shiqi Li, Jia Liu, and Zhiqun Cheng

Cite This: *ACS Appl. Nano Mater.* 2022, 5, 17048−17058 Read Online

ACCESS | Metrics & More | Article Recommendations | SI Supporting Information

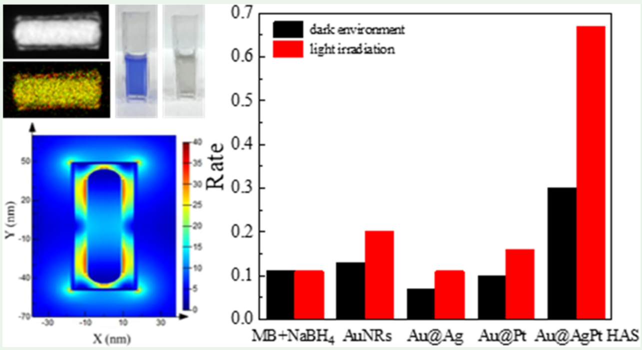

ABSTRACT: The localized surface plasmon resonances (LSPRs) in plasmonic nanoparticles have been used in accelerating photocatalytic reactions under light illumination. To improve the catalytic performance, bimetallic nanoparticles composed of a plasmonic core and a catalytic shell, where LSPR-excited hot electrons and the intrinsic catalytic active sites work synergistically, have attracted much attention. Despite progress in designing bimetallic catalysts, balancing the strong LSPR and catalytic sites remains challenging. Here, a trimetallic nanostructure containing a gold nanorod (AuNR) core and a silver−platinum (AgPt) hollow alloy shell was designed and used as a plasmon-mediated photocatalyst for methylene blue reduction reaction. Specifically, the AuNRs covered by a thin layer of Ag (Au@Ag) were used as the template to deposit Pt, forming a Au@AgPt trimetallic nanostructure. By changing the Ag and/or Pt precursor concentration, the external layer could be varied from AgPt heterostructure and AgPt hollow alloy shell to AuAgPt alloy dendrites. Using methylene blue as a model system, the photocatalytic reduction reaction was studied by adding the obtained nanoparticles as catalysts under visible and near-infrared light irradiation. The optimal photocatalytic performance of the trimetallic nanoparticles was seen with the AgPt hollow alloy shell, and the reaction rate is ∼7 times higher than that of the reaction without catalysts and ∼3 times higher than that of monometallic AuNRs, bimetallic Au@Ag, and Au@Pt nanorods. Plasmon energy transfer from the AuNRs to the AgPt layer, which enhances the charge-carrier generation, is responsible for outstanding photocatalytic performance. The approach used here to synthesize Au@AgPt trimetallic nanostructures is suitable for the design of other multimetallic photocatalysts.

KEYWORDS: *gold nanorods, nanoparticles, hollow alloy shell, trimetallic nanostructures, localized surface plasmon resonance, photocatalysis*

1. INTRODUCTION

Noble metal-based multimetallic nanoparticles have attracted enormous interest because of their intriguing size; shape; and composition-dependent catalytic, optical, electrical, and magnetic properties.[1−10] Among these properties, catalysis has been the hottest research topic in noble multimetallic-based nanoparticles since nanoparticles can combine the properties of two or more noble metal nanoparticles.[11−18]

Generally, the catalytic performance of noble metal nanoparticles can be divided into two categories. One category is the common plasmonic nanoparticles such as Au[19−21] and Ag,[22−24] while the other category is the common catalytic (nonplasmonic) Pd and Pt nanoparticles.[25−28] The plasmonic nanoparticles can support localized surface plasmon resonances (LSPRs): coherent oscillations of conduction electrons in a conductive medium. Thus, the LSPRs can create intense localized electric fields and hot electrons. The absorption cross section of the plasmonic nanoparticles can be ∼10^5 times larger than that of typical dye molecules.[29] More importantly, the plasmonic properties of these nanoparticles could be tuned across the entire visible and near-infrared spectrum, depending on the size, geometry, and material of the nanoparticle. The interaction of LSPR with adsorbate orbitals can lead to the injection of energized charge carriers into the adsorbate, resulting in chemical transformations. Linic's group[30] has proved this mechanism by coupling wavelength-dependent Stokes and anti-Stokes surface-enhanced Raman scattering (SERS) with kinetic analysis of photocatalytic reactions on a Ag nanocube and a methylene blue (MB) system. They propose that the LSPR-induced electric field results in a direct charge transfer within the molecule—adsorbate system. Therefore, plasmonic nanoparticles hold great promise for improving the efficiency of sunlight absorption.

Received: September 6, 2022
Accepted: November 1, 2022
Published: November 9, 2022

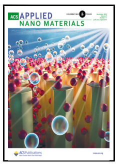

https://doi.org/10.1021/acsanm.2c03953
ACS Appl. Nano Mater. 2022, 5, 17048−17058

However, traditional plasmonic nanoparticle catalysts are only valid for a limited type of reactions, while common catalytic nanoparticles do not support strong LSPR at the visible and near-infrared regions, where sunlight irradiation is the strongest. Therefore, in many previous studies, bimetallic nanoparticles composed of a plasmonic core and a catalytic shell have shown superior catalytic performance.[31−40] For example, de Jongh et al.[39] designed a Au−Pd core−shell bimetallic catalyst and obtained synergistic catalytic performance in the selective hydrogenation of butadiene. Yang et al.[40] demonstrated that a Au−Pt bimetallic nanostructure could improve the photocatalytic performance of the *p*-nitrophenol reduction reaction compared to single monometallic nanoparticles.

However, Pd (or Pt) metal has a big imaginary part in the dielectric function, resulting in large plasmonic damping. When the plasmonic nanoparticles were covered by a Pd (or Pt) shell, the intensity of LSPR dramatically decreased and the width broadened,[41−44] since the LSPR of the core−shell nanostructure is mainly dependent on the materials in the shell. This large plasmonic damping will lead to poor catalytic performances. For instance, Cheng et al.[45] studied the catalytic performance of the Au nanoparticles covered with different shell thicknesses of Pd and found that a thicker shell led to a lower reaction rate. Besides, in the methods of the synthesis of trimetallic nanostructures, there are some shortcomings, such as high temperature[5,46] and long reaction time.[47,48] In the properties of the trimetallic nanostructures, most studies concentrated on electrocatalysis,[49−51] and there are few studies on photocatalysis in the trimetallic system. Thus, there is still a big challenge to design plasmon-mediated photocatalysts having a catalytic shell in trimetallic nanostructures while keeping the original strong LSPR property.

Herein, we propose a simple and reproducible method to synthesize trimetallic nanostructures with morphologies that can be controlled, and the photocatalytic performance can be greatly improved when gold nanorod (AuNR) core and AgPt hollow alloy shell (HAS) nanostructures are presented. In detail, in the synthesis of trimetallic core−shell noble metal-based nanoparticles, first, we synthesized the AuNRs by a seed-mediated method, coated a Ag shell on the surface of AuNRs, and finally used galvanic replacement with coreduction to form a Au@AgPt hollow alloy shell (Au@AgPt HAS) nanostructure. In terms of photocatalysis, we adopted the reaction of $NaBH_4$ reducing methylene blue (MB) by adding the abovementioned nanoparticles under light irradiation and monitored the reaction processes with UV−vis−NIR spectra. We selected nanoparticles with different morphologies for the photocatalytic reaction, and the experimental results show that Au@AgPt nanoparticles with HAS nanostructures have the best photocatalytic performance. Our strategy can be extended to synthesize other multimetallic nanostructures, which may represent a route for designing excellent plasmonic photocatalysts.

2. RESULTS AND DISCUSSION

The AuNRs were selected as the plasmonic core materials since their LSPRs can be easily tuned by the aspect ratio (length/diameter), and the spectrum is varied from ∼600 to >1200 nm, where the sunlight is the strongest.[52] We synthesized the AuNRs by a seed-mediated growth procedure with slight modification[53,54] (see the Experimental Section in the Supporting Information, SI). The obtained AuNRs with a size of 88.7 ± 7.0 nm length and 17.1 ± 1.7 nm width (Figure S1a) were used as seeds for the overgrowth of the Ag shell. By adding $AgNO_3$ and ascorbic acid (AA) to the AuNR aqueous solution, an Au@Ag core−shell cuboid structure was obtained, with a size of 98.8 ± 5.9 nm length and 33.8 ± 2.0 nm width (Figure S1b). Finally, K_2PtCl_4 was added to the Au@Ag solution, forming the Au@AgPt trimetallic nanostructures.

By fine-tuning the amount of $AgNO_3$ and/or K_2PtCl_4, three main morphologies of the final Au@AgPt nanoparticles were obtained (Scheme 1). For comparison of the catalytic performance, the Au@Pt NR sample was also prepared with an 88.1 ± 5.6 nm length and a 19.1 ± 1.6 nm width (Figure S1c). The UV−vis−NIR spectra of AuNRs, Au@Ag, and Au@Pt NRs are shown in Figure S1d. The intensity of LSPR increased after Ag overgrowth and decreased after Pt deposition. The whole process of synthesizing AgPt alloy can be limited to 20 min, which is a greatly reduced time compared with previous works.[47,48] Besides, the temperature of the reaction is kept at 60 °C, which is quite lower than those of previous synthesizing trimetallic nanostructures.[5,46]

Scheme 1. Illustration of the Synthesis Process of Au@AgPt Nanostructures[a]

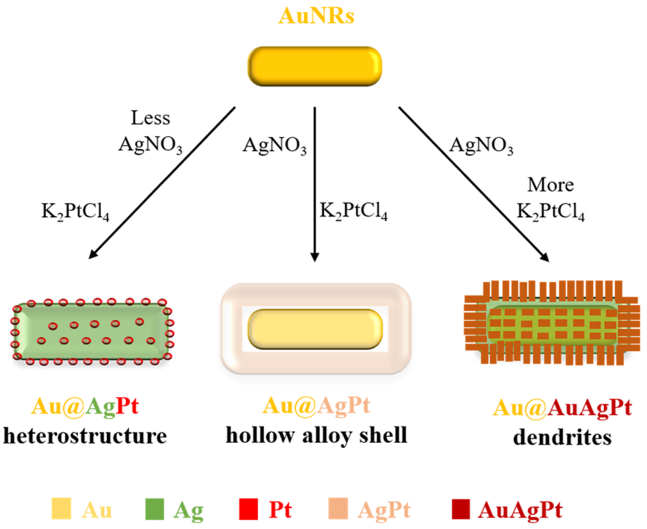

[a]There are three typical morphologies of the final products, which are Au@AgPt heterostructures, hollow alloy shells, and dendrites.

The reactants have been found to be important for the growth of the nanostructures with various shapes in our experiments. To understand the influence of precursor $AgNO_3$ on the final nanostructure, we selected different amounts of $AgNO_3$ (0.01−0.40 mL, 4.0 mM) for the experiments while keeping K_2PtCl_4 fixed (0.04 mL, 2.0 mM). All of the transmission electron microscopy (TEM) images and UV−vis−NIR spectra are shown in Figure S2. Generally, three types of morphologies could be obtained in the process of the synthesis. Figure 1a shows the schematic of the typical morphologies of Au@AgPt nanostructures with different amounts of $AgNO_3$. To understand the elemental distribution and crystalline structure of Au@AgPt nanostructures, energy-dispersive spectroscopy (EDS) elemental mapping and high-resolution transmission electron microscopy (HRTEM) were performed, as shown in Figures 1 and S3−S5. Au, Ag, and Pt in EDS mapping images were shown in yellow, green, and red, respectively. When 0.01 mL of $AgNO_3$ was used, Pt formed

https://doi.org/10.1021/acsanm.2c03953
ACS Appl. Nano Mater. 2022, 5, 17048−17058

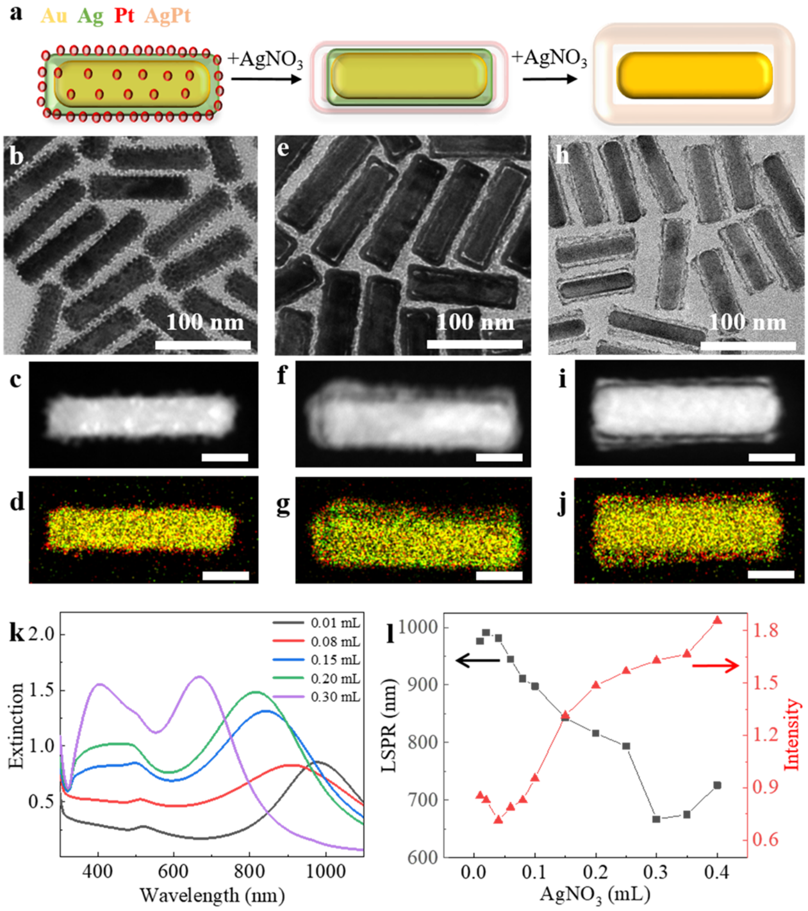

Figure 1. Morphology control of Au@AgPt nanostructure by tuning the amounts of $AgNO_3$ precursor. (a) Schematic of Au@AgPt with different amounts of $AgNO_3$. The amounts of $AgNO_3$ are 0.01 mL in (b−d), 0.08 mL in (e−g), and 0.20 mL in (h−j). (b, e, h) TEM images, (c, f, i) high-angle annular dark-field scanning transmission electron microscopy (HAADF-STEM) images, and (d, g, j) EDS mapping of the Au@AgPt nanostructures. Scale bars are 20 nm for all of the HAADF-STEM and EDS mapping images. (k) UV−vis−NIR spectra of Au@AgPt with different amounts of $AgNO_3$ from 0.01 to 0.30 mL. (l) LSPR and intensity of Au@AgPt with different amounts of $AgNO_3$. As the amount of $AgNO_3$ increased, the LSPR peaks gradually blue-shifted and the intensity increased.

granules on the surface of Au@Ag, resulting in a Au@AgPt heterostructure (Figure 1b−d). The crystal plane spacing of 0.200 nm is a family of Au {200} facets, and the spacing of 0.194 nm is the Pt {200} facets (Figure S4a). With the increase of $AgNO_3$, a fully covered shell was gradually formed on the surface, and then a hollow structure first appeared at the four corners. Figure 1e−g shows a typical sample at this stage ($AgNO_3$ 0.08 mL), where a AgPt smooth alloy shell starts to form. When the amount of $AgNO_3$ increased to 0.20 mL, a Au@AgPt hollow alloy shell (HAS) nanostructure was formed, as shown in Figure 1h−j. The Au@AgPt HAS is 99.8 ± 3.5 nm in length, 36.3 ± 2.4 nm in width, and 4.1 ± 0.7 nm in shell thickness. The crystal plane spacing of 0.200 nm corresponds to the Au {200} facets, and the crystal plane spacing of 0.189 nm belongs to AgPt {200} facets (Figure S4d,e). When the amount of $AgNO_3$ was greater than 0.20 mL, asymmetric Au@AgPt trimetallic structures were formed, resulting in the uneven morphology of the final nanostructure, and the morphology was uncontrollable (Figure S2i−k). Figure 1k shows UV−vis−NIR spectra of Au@AgPt nanoparticles as a function of $AgNO_3$ amount. With the increase of $AgNO_3$, the LSPR blue-shifted, and its intensity increased (Figure 1l). This is due to the higher energy of plasmonic resonance and less plasmonic damping of Ag material compared with pure Au.

In addition to $AgNO_3$, the change of the amount of K_2PtCl_4 also affects the final morphology of the Au@AgPt nanostructures. In these experiments, we added K_2PtCl_4 from 0.04 to 0.40 mL (2.0 mM) and kept fixed the amount of $AgNO_3$ (0.10 mL, 4.0 mM). All of the results are shown in Figures 2, S6, and S7. With the increase of K_2PtCl_4, the external layer started from a smooth shell (Figure S6a) and gradually changed to a dendritic structure (K_2PtCl_4 > 0.10 mL, Figure S6b−d). The thickness of the dendritic structures increased by further increasing the amount of K_2PtCl_4 (Figure S6e,f). Figure 2a shows the schematic of the two typical structures of Au@AgPt with different amounts of K_2PtCl_4. Figure 2b shows the HAADF-STEM and EDS mapping results of Au@AgPt nanostructure with 0.04 mL of K_2PtCl_4. The elemental distribution of Au (yellow), Ag (green), and Pt (red) of the square area (in Figure 2b) of a single Au@AgPt nanostructure is shown in Figure 2c, indicating that AgPt formed a smooth alloy shell, similar to the results of Figure 1e,f. Figure 2d,e shows the dendritic layer with 0.20 mL of K_2PtCl_4. We found that both Au and Ag appeared in the dendritic layer (Figures 2e and S6). The circled part in Figure 2e indicated that Au was also distributed in the outer layer. Thus, the final structure should be Au@AuAgPt alloy dendrites. HRTEM images (combined with the EDS mapping) of both samples show the crystal plane spacing of 0.189 nm at the outer layer,

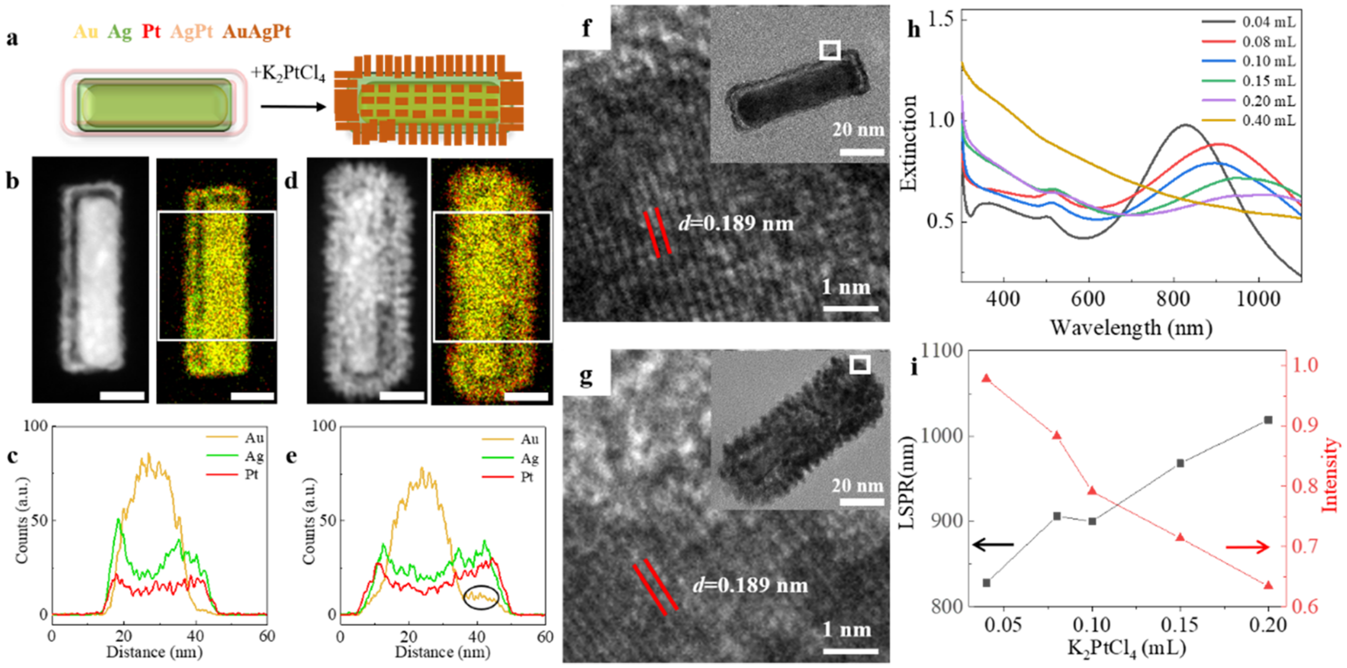

Figure 2. Morphology control of Au@AgPt nanostructure by tuning the amounts of K_2PtCl_4. (a) Schematic of Au@AgPt with different amounts of K_2PtCl_4. The amounts of K_2PtCl_4 are 0.04 mL in (b, c, f) and 0.20 mL in (d, e, g). (b) HAADF-STEM image and EDS mapping of a single Au@AgPt with 0.04 mL of K_2PtCl_4. Scale bars are 20 nm. (c) The elemental distribution of Au (yellow), Ag (green), and Pt (red) in the white box area of (b). (d) HAADF-STEM and EDS mapping images of a single Au@AgPt with 0.20 mL of K_2PtCl_4. Scale bars are 20 nm. (e) The distribution of three elements in the box area of (d). The circle indicates that Au appeared in the dendritic layer. (f, g) HRTEM images of the Au@AgPt nanostructures with K_2PtCl_4 of 0.04 mL (f) and 0.20 mL (g). Both of the crystal plane spacings of the shell are 0.189 nm. (h) UV−vis−NIR spectra of Au@AgPt with K_2PtCl_4 amounts from 0.04 to 0.40 mL. (i) LSPR and intensity of Au@AgPt with different amounts of K_2PtCl_4. As the amount of K_2PtCl_4 increased, the LSPR peaks gradually red-shifted and the intensity decreased.

corresponding to the Pt {200} facets (Figure S7), which indicates that the Pt lattices dominate the AgPt (Figure 2f) and AuAgPt (Figure 2g) alloy nanostructures. The UV−vis−NIR spectra of Au@AgPt by controlling K_2PtCl_4 are shown in Figure 2h. It can be seen that with the increase of the amount of K_2PtCl_4, the spectrum gradually red-shifts, the longitudinal peak widens, and the intensity gradually decreases (Figure 2i). This is due to the large imaginary part of dielectric function in Pt material, resulting in significant plasmonic damping. The LSPR even disappeared when K_2PtCl_4 increased to 0.40 mL (Figure 2h, brown curve). Thus, different structures could be obtained by simply tuning the amount of $AgNO_3$ and K_2PtCl_4 precursors. It is important to understand the growth processes (mechanism), which will be discussed below.

In our synthesis, the first step is to use AuNRs as seeds to deposit Ag. Owing to the lattice match between Au (4.08 Å) and Ag (4.09 Å), Ag can epitaxially grow on the surface of Au, forming Au@Ag bimetallic NRs with single crystalline structures.[44] The second step is to use Au@Ag as a template to deposit Pt, forming Au@AgPt trimetallic nanostructures. Ag^+ has a relatively lower reduction potential as compared with Pt^{2+}. Thus, the galvanic replacement occurs once a K_2PtCl_4 aqueous solution is introduced to the suspension of Au@Ag NRs. In this galvanic reaction, Ag atoms are gradually oxidized to Ag^+ ions, while the generated electrons are quickly captured by Pt^{2+} ions to produce Pt atoms through a reduction process. The overall reaction processes are summarized as follows:

$$2Ag + PtCl_4^- \rightarrow 2Ag^+ + Pt + 4Cl^- \tag{1}$$

Both the precursor Pt^{2+} and the newly yielded Ag^+ ions were coreduced to atoms by ascorbic acid, and the generated Pt and Ag atoms were codeposited on the Au@Ag NRs, forming a AgPt alloy shell. As the reaction proceeded, the interior Ag was gradually exhausted through the galvanic replacement reaction, eventually forming a AgPt hollow alloy shell (Figure 1h−j).

A notable example of a previous work by Xia et al.[55] was the galvanic replacement reaction between Ag nanocubes and $HAuCl_4$. They observed that the reaction was generally initiated at those sites of the Ag nanocubes with defects, stacking faults, or steps that possess the highest surface energy. In the reaction, Ag atoms were oxidized and dissolved into solution, while the Au^{3+} were reduced and Au atoms were produced and deposited on the surface of the Ag nanocube template. During this process, an incomplete layer of Au on the Ag template was formed, and finally, a Au−Ag nanocage was obtained. Previous works on combining galvanic replacement and coreduction reactions were also reported for producing hollow alloy nanostructures, e.g., Pd−Pt nanocages,[56,57] Au−Ag nanocages,[58] and ultrathin Pt−Ag nanocubes.[59]

According to these previous reports and discussions,[55−59] it is believed that a thin but incomplete layer of Pt on the Au@Ag template was formed at the early stages. At the same time, some formed pits on the surface, accompanying the successive Pt deposition, and can serve as the reaction channel for dissolving Ag continuously. When less $AgNO_3$ was used, Ag was exhausted quickly at the early stage after adding K_2PtCl_4, and then Ag^+ and Pt^{2+} were both reduced by AA to produce Ag and Pt atoms, respectively. Since the relatively large lattice mismatch of Pt (3.92 Å) compared to Au and Ag, the newly yielded Ag atoms tend to epitaxially deposit on the surface of Au, while Pt forms granules at the surface, resulting in a Au@AgPt heterostructure (Figure 1b−d). In the previous work on

https://doi.org/10.1021/acsanm.2c03953
ACS Appl. Nano Mater. 2022, 5, 17048−17058

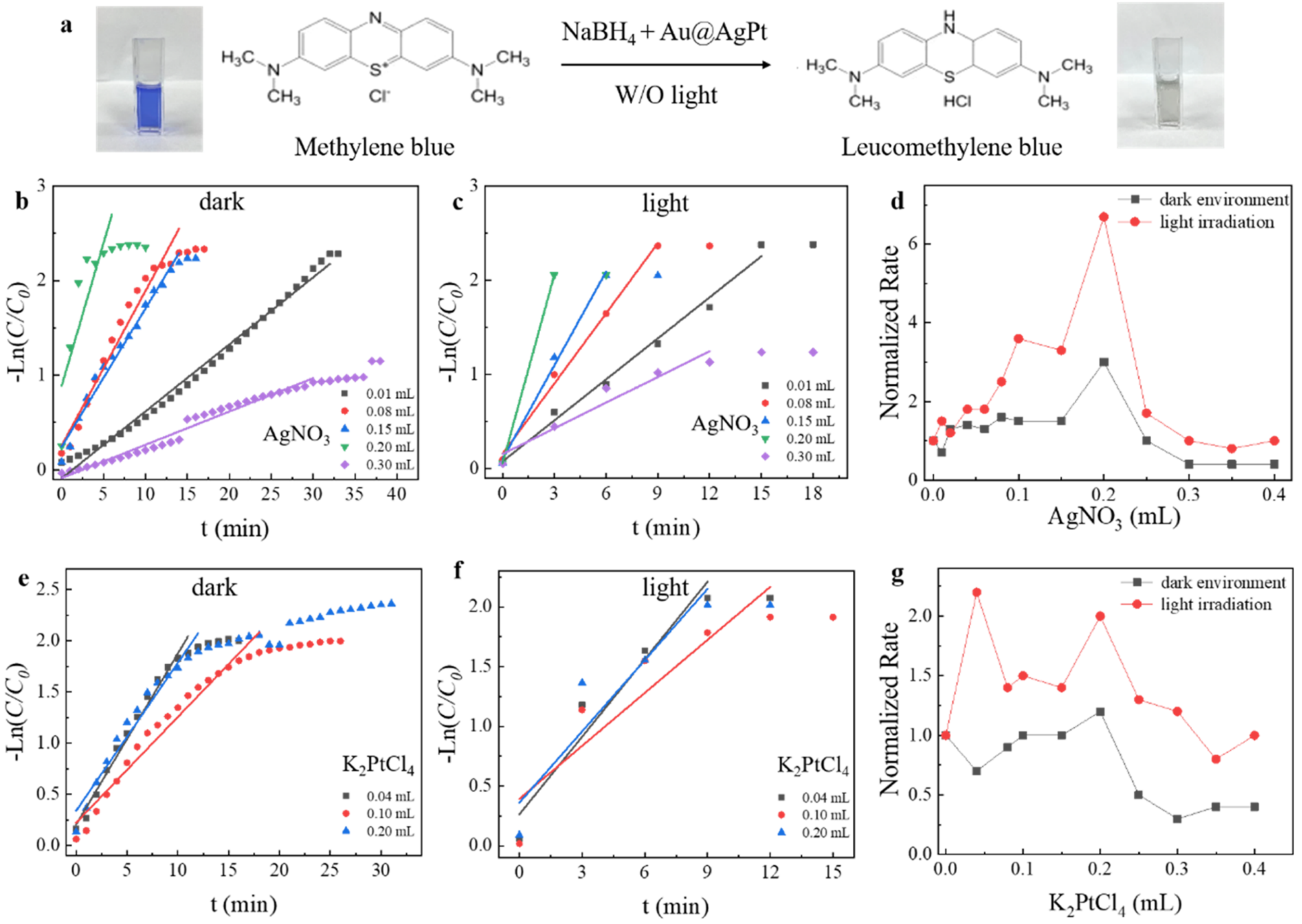

Figure 3. Plasmon-enhanced catalytic and photocatalytic performances of Au@AgPt with different nanostructures. (a) Scheme of MB reduced by $NaBH_4$ without or with light. The C═S and C═N bonds in the MB formula broke under the reduction of $NaBH_4$, and the color of the solution became colorless. Au@AgPt with different $AgNO_3$ precursors were used in (b) catalysis and (c) photocatalysis. (d) Reaction rates of different nanostructures with different amounts of $AgNO_3$ catalyzed by dark and light conditions, respectively. Au@AgPt used in (e) catalysis and (f) photocatalysis with different K_2PtCl_4 precursors. (g) Reaction rates of different nanostructures with different amounts of K_2PtCl_4 catalyzed by dark and light conditions, respectively. It should be noted that 0 mL of $AgNO_3$ refers to the reduction of MB by $NaBH_4$ alone. Pearson's coefficient of the reaction rate under light illumination and in the dark in Figure 3d,g is listed in Tables S2 and S3.

Pt overgrowth on Au, the authors found that Pt^{2+} ions can oxidize the Au template, and the etched-Au structures were found in their results.[60] Therefore, when a higher K_2PtCl_4 amount was used, after the Ag was exhausted, the excess Pt^{2+} ions can further oxidize (etch) Au, and the galvanic replacement and coreduction of Pt and Au metals occurred simultaneously, resulting in a AuAgPt alloy structure (Figure 2d). The evidence that Au was partially dissolved with excess Pt^{2+} ions can be found in the elemental distribution in Figure 2e (indicated by the circle) and the EDS mapping images in Figure S7j,n. As indicated by the circle in Figure 2e, there is a shoulder in the elemental distribution, which is different as less amount of K_2PtCl_4 was used. The net counts of EDS are provided in Figure S8. The three typical Au@AgPt nanostructures are summarized in Scheme 1.

For control experiments, we also investigated the effects of reaction speed on the final products, which could be controlled by the reaction temperature and AA. When controlling the temperature, we selected 40, 60, and 80 °C for comparison (Figure S9). Compared with the temperature condition of 60 °C, some hollow structures appeared at 40 °C, but the morphology of the final product was not uniform (Figure S9a), and basically, only a few hollow structures appeared at 80 °C (Figure S9b). Moreover, different amounts of AA were used to investigate the effect of AA on the final structure (Figure S10). The results showed that the morphology of the final product was the most uniform by adding increased amounts of AA (0.05 mL, 100 mM). Thus, it is important to manipulate the rates of galvanic replacement and coreduction reactions in the synthesis.

To investigate the plasmon-mediated photocatalytic activity of the Au@AgPt trimetallic nanostructures, we chose the reduction of methylene blue (MB) with $NaBH_4$ as a model reaction system under light irradiation by a Xe lamp ($\lambda > 420$ nm). After the reduction, MB changes to a reduced MB state (leucomethylene blue), where the color is changed from blue to colorless (Figure 3a). During the reaction, vis−NIR spectra were recorded as a function of the reaction time. The reaction times of MB reduced by $NaBH_4$ are 40 min and 36 min in the dark and light conditions, respectively (Figure S11a,b). Progress of the reaction was monitored by the intensity of the characteristic extinction peak of MB at $\lambda_{max} = 630$ nm with reaction time. C_0 refers to the peak value corresponding to the initial MB at $t = 0$ min, and C is the peak value of 630 nm

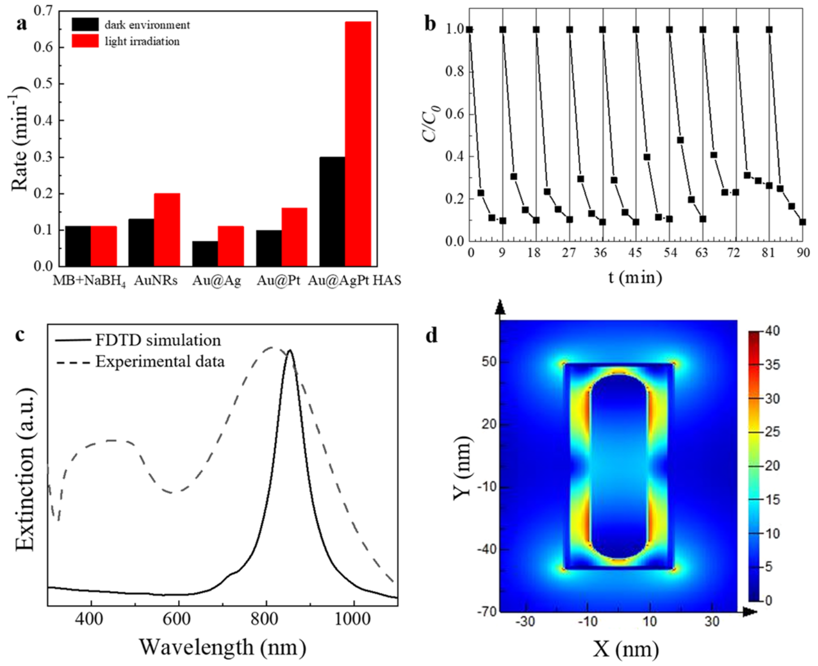

Figure 4. Photocatalytic reaction rate, photocatalytic cycle experiments, and finite-difference time domain (FDTD) simulations. (a) Plasmon-enhanced catalysis performances of varied nanostructures under both dark (black bars) and light irradiation (red bars). Compared with other catalysts, the Au@AgPt HAS nanostructures show excellent catalytic performance under dark and light conditions. (b) Cyclic curves of Au@AgPt nanostructures in photocatalysis with 0.15 mL of $AgNO_3$ and 0.04 mL of K_2PtCl_4, and 10 photocatalytic cycles of 9 min were performed. (c) Simulated (solid line) and experimental (dashed line) spectra of a single Au@AgPt HAS nanostructure. The size parameters of the Au@AgPt HAS in simulation were obtained from the experimental data, which were 99 nm in length, 36 nm in width, and 4 nm in shell thickness, and the size of AuNR inside is 88 nm in length and 17 nm in width. Only longitudinal LSPR was calculated by setting the polarization parallel to the long axis of the nanostructure (Y axis in d). The simulated spectra are in good agreement with the experimental data. The broadening in experimental spectra is due to the polydispersity of AuNR size and AgPt alloy shell thickness. (d) Electric field distribution of a single Au@AgPt HAS. The hot spots are located in the vicinity of the AuNR and at the four vertices of the AgPt outer layer.

measured at an appropriate time interval during the reaction process. All of the spectra for catalytic reactions with different morphologies of trimetallic nanostructures are shown in Figures S12−S16. Then, we calculated the $-\mathrm{Ln}(C/C_0)-t$ curve in Figure 3b,c,e,f. Figure 3b,c shows the reaction rates when the trimetallic nanostructures obtained by changing the amount of $AgNO_3$ were used as catalysts under dark and light illumination. The catalytic rates of Au@AgPt with different morphologies were calculated and normalized by the catalytic rate of MB + $NaBH_4$ without nanoparticles (Figure 3d). In these experiments of Au@AgPt by changing the amount of $AgNO_3$ for catalysis, the catalytic rate of the Au@AgPt HAS is the best, which was ∼7 times higher than that of the reaction without catalysts under the light condition (∼3 times higher than that under the dark condition). Figure 3e,f shows the reaction rates when the trimetallic nanostructures are obtained by changing the amount of K_2PtCl_4, and Figure 3g shows the catalytic rate curve by changing the amount of K_2PtCl_4. The rate curve is M-shaped due to the occurrence of two optimal values in 0.04 and 0.20 mL of K_2PtCl_4.

To compare the catalytic performance of Au@AgPt HAS nanostructure with single metallic or bimetallic nanoparticles, we used AuNRs, Au@Ag NRs, and Au@Pt NRs (Figure S16) to catalyze the MB reduction reaction. In the dark environment, the reaction time of AuNRs, Au@Ag, and Au@Pt was 30, 29, and 25 min, while it was 18, 21, and 18 min under light irradiation, respectively. The curves of the catalytic rate are shown in Figure S17. The Au@AgPt HAS was used as a catalyst both in dark and light conditions, and the response time was 3 min in light and 6 min in the dark. It can be observed that the reaction time is greatly shortened and the catalytic rate is greatly strengthened under the light condition. Figure 4a shows the catalytic rate of different nanoparticles; it indicates that the catalytic efficiency of Au@AgPt HAS is the best both under dark and light illuminations.

Since Au, Ag, and Pt metals are expensive, to save costs, we have performed a catalytic cycle test. Considering the reaction time and reaction rate, we selected Au@AgPt with 0.15 mL of $AgNO_3$ and 0.04 mL of K_2PtCl_4 to perform the photocatalytic experiments. A total of 10 photocatalytic cycles were carried out, and centrifugal cleaning was performed twice at the end of each photocatalytic cycle. The experimental results show that after 10 cycles of photocatalytic reactions, the final catalytic efficiency is still very close to that of the first cycle (Figure 4b). We measured the extinction spectrum and performed TEM of the Au@AgPt sample after 10 rounds of photocatalytic reactions, as shown in Figure S18. There is no significant difference in the spectra before and after 10 catalytic cycles, and the TEM images show that the nanostructure of Au@AgPt has no influence after 10 photocatalytic cycles. Compared with an inexpensive semiconductor such as TiO_2, which has a wide band gap that allows it to be excited only by ultraviolet light, Au@AgPt can be recycled and has broad-band LSPRs, which possess the potential to be excited by sunlight. This can save costs to some extent, especially in the cost and power consumption of large industrial fields. Therefore, the Au@AgPt catalysts can be reused and have the potential for practical catalytic reactions.

In the catalytic experiments of different noble metal-based nanostructures, both dark conditions and light illumination can dramatically increase the reaction rate, especially for the Au@AgPt HAS nanostructure. In the dark condition, Au@AgPt HAS shows the best catalytic performance compared to other nanostructures, causing the Au@AgPt HAS to have a larger area among the other structures, which offers more area to contact the reactant. The ends of Au@AgPt are exposed in the solution, and the MB molecule can enter the inner sides. Therefore, the Au@AgPt HAS offers more active sites to catalyze the reaction.

To find out why the Au@AgPt HAS showed such superior performance in photocatalysis, we performed FDTD simulations for calculating the spectrum and electric near-field distributions at the catalytic interface for a single Au@AgPt HAS nanostructure. Figure 4c shows the simulated extinction spectra (solid line), which are consistent with the experimental results (dashed line). Due to the polydispersity, shell thickness, and the Ag-to-Pt ratio of the nanostructure, the width of the peaks is broadened in the experimental spectrum. As control simulations, the extinction spectra as a function of AgPt shell thickness (3−6 nm) were simulated. As shown in Figure S19, the LSPR blue-shifted with the increase of the AgPt shell thickness. Figure 4d shows the electric field distribution of a single Au@AgPt HAS, with two obvious superiorities (hot spots). One is in the vicinity of the AuNRs, while the other is at the four corners of the AgPt hollow alloy shell. We also simulated the electric field distribution of a core−shell structure of Au@AgPt (Figure S20). The field enhancement only appeared at the four corners, and the intensity is much lower than that of the Au@AgPt HAS (Figure 4d). In addition to the thickness of the AgPt alloy shell, we also simulated the spectra and electric field of different Ag-to-Pt ratios in the AgPt alloy (Figures S22 and S23). With the increase of Pt%, the LSPR blue-shifted from 887 to 797 nm (Figure S22), and the intensity of the electric near-field decreased (Figure S23). In a previous work, it was also seen that the photocatalytic performance depended on the wavelength of the light irradiation.[61] Since our work focused more on the structural differences in the reaction rates, the effects of the above-mentioned parameters on the photocatalytic reactions will be investigated in future work.

Thus, we propose the mechanism of plasmon-mediated photocatalysis as follows. First, under light irradiation, hot electrons could be generated in the inner AuNRs or some residue Ag in the gap between the inner AuNRs and AgPt alloy. Then, holes are formed, the excited electrons and the resulting holes form electron−hole pairs,[21,62] and Pt could be the medium for hot electron transport. Next, the hot electrons could be injected into the reaction of MB reduced by $NaBH_4$. In addition, Ag can also generate hot electrons and transfer them to the Pt in the AgPt alloy, which greatly reduces the time of reaction. Previous work by Zhu's group[63] also claimed the combination of light absorption of AuPd alloy nanoparticles. The enhanced interaction and the intrinsic catalytic activity of the transition metal lead to a unique structure where the absorption of light can yield energetic electrons. Second, the Au and Ag with surface plasmon resonance properties can produce heat when exposed to light, increasing the temperature of the reaction and thus improving the energy of the reaction and playing a catalytic role.[64] As an AgPt alloy on the surface of AuNRs, Ag is also a metal with surface plasmon resonance, which can produce heat under light irradiation. Thus, heating the AgPt alloy can improve the reaction rates of photocatalysis. Third, the hollow structure can provide a greater contact area. In these interstices, the intensity of the electric field is stronger under light irradiation, and the AgPt alloy is not compact, which can also be contacted with the reactant. Therefore, the performance of photocatalysis can be improved. In the model of the Au@AgPt HAS catalysis, the outer AgPt alloy's shell thickness, and Ag-to-Pt atomic ratio should also influence the photocatalytic reaction rates, and this will be investigated in the future.

3. CONCLUSIONS

We have demonstrated a simple and reproducible method for the synthesis of Au@AgPt trimetallic nanostructures. By systematically tuning the amount of $AgNO_3$ and K_2PtCl_4 precursors, the shell nanostructures could be varied from AgPt heterostructure, AgPt hollow alloy shell, and AuAgPt dendrites. In other words, we have realized controllable trimetallic morphologies with the same reactant by simply tuning their amounts. In the three morphologies, Au@AgPt HAS shows the best catalytic performance (in the reduction of MB assisted by $NaBH_4$) in both dark conditions and light irradiation. Under the dark condition, the catalytic rate of Au@AgPt HAS is ∼3 times that of a noncatalyst and ∼2 times that of monometallic AuNRs, bimetallic Au@Ag, and Au@Pt nanorods. Under light irradiation, due to the larger active area and high hot electron transfer efficiency, the photocatalytic reaction rate of Au@AgPt HAS is ∼7 times higher than that of the reaction without catalysts and ∼3 times higher than that of monometallic AuNRs, bimetallic Au@Ag, and Au@Pt nanorods. FDTD simulations carried out on the electric near-field distribution confirmed that the hot spots of Au@AgPt HAS are in the vicinity of AuNRs and at the four corners of the AgPt hollow alloy shell, which would enhance the photocatalytic performance. In addition, Au@AgPt can be recycled and it retains the same catalytic performance after 10 cycles, which can greatly save the cost and practically contribute to environmental protection. Finally, we demonstrate the genuine superiority of the trimetallic nanostructures, especially hollow alloy nanostructures, in the plasmon-mediated photocatalytic reactions, which will offer useful guidelines to design and construct high-performance plasmon-based catalysts, sensors, and devices in the future.

4. EXPERIMENTAL SECTION

4.1. Materials. All chemicals were used as received without further purification. Hexadecyltrimethylammonium bromide (CTAB, >99.0%), L-ascorbic acid (AA, >99.99%), chloroauric acid ($HAuCl_4$), hydrochloric acid (HCl, 37 wt % in water), and methyl blue (MB) were purchased from Macklin. Hexadecyltrimethylammonium chloride (CTAC, >99.0%), sodium borohydride ($NaBH_4$, 98%), sodium oleate (NaOL, >99.8%), silver nitrate ($AgNO_3$, >99.8%), and potassium tetrachloroplatinate(II) (K_2PtCl_4, >99.99%) were purchased from Aladdin. Ultrapure water (Millipore Milli-Q grade) with a resistivity of 18.2 MΩ was used in all of the experiments. All glassware for the gold nanorod synthesis was cleaned with freshly prepared aqua regia (HCl/HNO_3 in a 3:1 volume ratio), rinsed with large amounts of water, and dried at 60 °C before usage.

4.2. Synthesis of Gold Nanorods (AuNRs). AuNRs with an aspect ratio of 4.7 were prepared following a seed-mediated growth procedure previously reported by Murray et al.[53] The seed solution for gold nanorod growth was prepared as follows: first, 0.25 mL of 10.0 mM $HAuCl_4$ was added to 10.0 mL of 0.1 M CTAB solution. Then, 0.6 mL of 10.0 mM $NaBH_4$ (freshly prepared with cold water) was added to the above solution under vigorous stirring (1200 rpm), which was stopped after 2 min. The color of the solution changed from light yellow to brownish. Finally, the seed solution was aged at 30 °C for 30 min before use.

To prepare the growth solution, 7.0 g (~37 mM in the final growth solution) of CTAB and 1.24 g of NaOL were mixed in 250 mL of warm water (50 °C). Then, 18.0 mL of 4.0 mM $AgNO_3$ was added to the solution and kept undisturbed at 30 °C for 15 min. Afterward, 250 mL of 1.0 mM $HAuCl_4$ solution was added and stirred at 700 rpm. The resulting solution became colorless after 90 min. Next, 2.1 mL of HCl (37 wt % in water) was injected and stirred at 700 rpm for 15 min. After 15 min, 1.25 mL of 64.0 mM ascorbic acid was added to the solution above and vigorously stirred for 30 s before the addition of 0.8 mL of the seed solution. The resulting mixture was stirred for 30 s and left undisturbed at 30 °C for 12 h for AuNR growth.

4.3. Synthesis of Au@AgPt Nanostructures. The as-prepared AuNR solution was about 500 mL. Then, the AuNRs were purified twice by centrifugation at 7000 rpm for 30 min, followed by the removal of the supernatant. The resulting solution (concentrated 10 times) was kept in 2.0 mM CTAB as the stock solution. To deposit Ag on the surface of AuNRs, 0.1 mL of the AuNR stock solution was added to the mixed solution, which contained 3.4 mL of 30.0 mM CTAC. The mixed solution was heated in a 60 °C water bath for 20 min. Then, 0.05 mL of 100 mM AA and 0.2 mL of 4.0 mM $AgNO_3$ were added to the solution and kept in a 60 °C water bath for 30 min. Then, the Au@Ag nanostructures can be obtained. Finally, 0.04 mL of 2.0 mM K_2PtCl_4 was added to the Au@Ag solution and kept in a 60 °C water bath for 20 min. The solution was then collected after two centrifugation cycles at 7000 rpm for 30 min. To obtain different morphologies of Au@AgPt nanostructures, we adjust the amounts of $AgNO_3$ (from 0.01 to 0.40 mL), K_2PtCl_4 (from 0.04 to 0.40 mL), and AA and reaction temperature. The detailed experimental parameters can be found in Table S1.

4.4. Characterization. Optical extinction spectra were recorded with a UV-1900i spectrophotometer (Shimadzu, Japan) with a 10-mm optical path. The transmission electron microscopy (TEM) images were obtained with an HT-7700 microscope (Hitachi, Japan) operating at a voltage of 100 kV. High-resolution TEM (HRTEM) images and energy-dispersive spectroscopy (EDS) mapping were performed using a Talos F200S TEM with a 200 KV acceleration voltage. The particle sizes of the nanoparticles were measured from TEM images using ImageJ software, whereby >100 nanoparticles were measured for each sample.

4.5. Catalysis. Briefly, 1.0 mL of 0.05 mM MB was mixed with 0.03 mL of 0.5 M freshly prepared $NaBH_4$, and then different kinds of Au@AgPt (0.05 mL) solutions or 0.05 mL of AuNR solution were added to the mixed solution. We measured the extinction spectra of the solution at 1 min intervals until the peak corresponding to 630 nm disappeared. The color of the solution changes from blue to transparent.

4.6. Photocatalysis. Briefly, 1 mL of 0.05 mM MB was mixed with 0.03 mL of 0.5 M freshly prepared $NaBH_4$, then different kinds of Au@AgPt (0.05 mL) solutions or 0.05 mL of AuNR solution were added to the mixed solution above. We used the above catalytic experimental steps on the basis of the illumination with a 250 W Xenon lamp (HDL-II, Suzhou Betical Optoelectronics Technology Co. Ltd, China) equipped with a filter in which the light less than 420 nm was cut off. We measured the extinction spectra of the solution at 3 min intervals until the peak corresponding to 630 nm disappeared. The MB concentration was determined at the wavelength of 630 nm using a UV–vis spectrophotometer (UV-1900i, Shimadzu). The reaction was maintained at normal atmospheric temperature. For the cycling test, the catalysts were obtained by centrifugation and redispersed in a $MB/NaBH_4$ system. The cycling test was carried out under the same conditions.

4.7. FDTD Simulations. Finite-difference time domain (FDTD) is a method for solving Maxwell's equations on a discretized spatial grid in complex geometries. The FDTD simulations were carried out with commercial software (Lumerical FDTD Solutions). A total field scattered field source was used to simulate a propagating plane wave interacting with the nanostructures, with a wavelength range of 300–1100 nm. A three-dimensional nonuniform mesh was used, and a grid size of 1 nm was chosen for calculating the spectra and 0.5 nm for calculating the electric field distribution of Au@AgPt HAS. For the dimensions of Au@AgPt HAS, the average sizes as determined from TEM were used. The dielectric functions of Au were obtained by fitting the points from the data of Palik,[65] and the dielectric function of Ag and Pt were obtained from the data of Werner et al.[66] We calculated the effective dielectric functions of the AgPt alloy by the effective medium approximation (EMA) based on the Maxwell–Garnett equation[67]

$$P\frac{\varepsilon_{\mathrm{eff}} - \varepsilon_{\mathrm{Ag}}}{\varepsilon_{\mathrm{eff}} + 2\varepsilon_{\mathrm{Ag}}} + (1 - P)\frac{\varepsilon_{\mathrm{Pt}} - \varepsilon_{\mathrm{Ag}}}{\varepsilon_{\mathrm{Pt}} + 2\varepsilon_{\mathrm{Ag}}} = 0 \tag{2}$$

Thus, the effective dielectric functions of AgPt alloy are given by

$$\varepsilon_{\mathrm{eff}} = \varepsilon_{\mathrm{Ag}}\frac{2P(\varepsilon_{\mathrm{Pt}} - \varepsilon_{\mathrm{Ag}}) + \varepsilon_{\mathrm{Pt}} + 2\varepsilon_{\mathrm{Ag}}}{2\varepsilon_{\mathrm{Ag}} + \varepsilon_{\mathrm{Pt}} - P(\varepsilon_{\mathrm{Pt}} - \varepsilon_{\mathrm{Ag}})} \tag{3}$$

where $\varepsilon_{\mathrm{Pt}}$, $\varepsilon_{\mathrm{Ag}}$, and $\varepsilon_{\mathrm{eff}}$ are the dielectric functions of Pt, Ag, and the composite system (AgPt alloy), respectively. P is the proportion of Pt in the AgPt alloy, which could be obtained from the EDS mapping (P = 42% for AgPt HAS). Once the $\varepsilon_{\mathrm{eff}}$ was calculated by eq 3, it was imported into FDTD software. The real and imaginary parts of $\varepsilon_{\mathrm{eff}}$ are drawn in Figure S21. To investigate the effect of the Ag-to-Pt ratios on the plasmonic properties, we also performed an FDTD simulation by tuning the Ag-to-Pt ratio with a 10% interval. The simulated spectra and electric field distribution are shown in Figures S22 and S23, respectively.

■ ASSOCIATED CONTENT

Supporting Information

The Supporting Information is available free of charge at https://pubs.acs.org/doi/10.1021/acsanm.2c03953.

> Details of the experimental section and FDTD simulations; complete TEM images of Au@AgPt trimetallic nanostructures with different amounts of $AgNO_3$, K_2PtCl_4, and AA and reaction temperature; more HRTEM images and EDS mapping of Au@AgPt nanostructures; UV–vis–NIR spectra of the process of MB reduction as a function of time and reaction rate analysis, including AuNRs, Au@Ag NRs, Au@Pt NRs, Au@AgPt nanostructures, under both dark and light irradiation; FDTD simulations of Au@AgPt hollow alloy shell nanostructures with different shell thicknesses and Ag-to-Pt ratios; electric field distribution of solid Au@AgPt nanostructures; complete list of the samples at different synthesis conditions; and the dielectric function of AgPt alloy with different Ag/Pt ratios (PDF)

■ AUTHOR INFORMATION

Corresponding Author

Tian-Song Deng – *School of Electronics and Information Engineering, Hangzhou Dianzi University, Hangzhou 310018, P. R. China*; orcid.org/0000-0002-0841-4932; Email: dengts@pku.edu.cn

Authors

Qi Zhang – *School of Electronics and Information Engineering, Hangzhou Dianzi University, Hangzhou 310018, P. R. China*

Yun-Qi Dou – *School of Electronics and Information Engineering, Hangzhou Dianzi University, Hangzhou 310018, P. R. China*

Ming-Zhang Wei − *School of Electronics and Information Engineering, Hangzhou Dianzi University, Hangzhou 310018, P. R. China*

Shiqi Li − *School of Electronics and Information Engineering, Hangzhou Dianzi University, Hangzhou 310018, P. R. China*

Jia Liu − *College of Materials and Environmental Engineering, Hangzhou Dianzi University, Hangzhou 310018, P. R. China*

Zhiqun Cheng − *School of Electronics and Information Engineering, Hangzhou Dianzi University, Hangzhou 310018, P. R. China*

Complete contact information is available at: https://pubs.acs.org/10.1021/acsanm.2c03953

Notes

The authors declare no competing financial interest.

ACKNOWLEDGMENTS

The authors thank Meiyan Jiang at Zhejiang University of Technology and Sudan Shen at State Key Laboratory of Chemical Engineering (Zhejiang University) for their transmission electron microscopy support. T.-S.D. acknowledges financial support from the National Natural Science Foundation of China (NSFC, Grant No. 61905056). This work was also supported by the National Key R&D Program of China (Grant No. 2018YFE0207500), the National Natural Science Foundation (Grant Nos. 91938201 and 61871169), Zhejiang Provincial Natural Science Foundation (Grant Nos. LZ20F010004 and LY19E020011), and Project of Ministry of Science and Technology (Grant D20011).

REFERENCES

(1) Zhou, M.; Li, C.; Fang, J. Y. Noble-Metal Based Random Alloy and Intermetallic Nanocrystals: Syntheses and Applications. *Chem. Rev.* **2021**, *121*, 736−795.

(2) Bu, Y. Y.; Huang, R. Q.; Li, Z.; Zhang, P.; Zhang, L. J.; Yang, Y.; Liu, Z.; Guo, K. J.; Gao, F. L. Anisotropic Truncated Octahedral Au with Pt Deposition on Arris for Localized Surface Plasmon Resonance-Enhanced Photothermal and Photodynamic Therapy of Osteosarcoma. *ACS Appl. Mater. Interfaces* **2021**, *13*, 35328−35341.

(3) Fang, P. P.; Duan, S.; Lin, X. D.; Anema, J. R.; Li, J. F.; Buriez, O.; Ding, Y.; Fan, F. R.; Wu, D. Y.; Ren, B.; Wang, Z. L.; Amatore, C.; Tian, Z. Q. Tailoring Au-core Pd-shell Pt-cluster nanoparticles for enhanced electrocatalytic activity. *Chem. Sci.* **2011**, *2*, 531−539.

(4) Ma, Y. Y.; Li, W. Y.; Cho, E. C.; Li, Z. Y.; Yu, T. K.; Zeng, J.; Xie, Z. X.; Xia, Y. N. Au@Ag Core-Shell Nanocubes with Finely Tuned and Well-Controlled Sizes, Shell Thicknesses, and Optical Properties. *ACS Nano* **2010**, *4*, 6725−6734.

(5) Bich Quyen, T. T.; Su, W. N.; Chen, C. H.; Rick, J.; Liu, J. Y.; Hwang, B. J. Novel Ag/Au/Pt trimetallic nanocages used with surface-enhanced Raman scattering for trace fluorescent dye detection. *J. Mater. Chem. B* **2014**, *2*, 5550−5557.

(6) Qu, A. H.; Xu, L. G.; Sun, M. Z.; Liu, L. Q.; Kuang, H.; Xu, C. L. Photoactive Hybrid AuNR-Pt@Ag2S Core-Satellite Nanostructures for Near-Infrared Quantitive Cell Imaging. *Adv. Funct. Mater.* **2017**, *27*, No. 1703408.

(7) Xie, X. B.; van Huis, M. A.; van Blaaderen, A. Symmetric and asymmetric epitaxial growth of metals (Ag, Pd, and Pt) onto Au nanotriangles: effects of reductants and plasmonic properties. *Nanoscale* **2021**, *13*, 2902−2913.

(8) Forcherio, G. T.; Baker, D. R.; Leff, A. C.; Boltersdorf, J.; McClure, J. P.; Grew, K. N.; Lundgreni, C. A. Photodeposition of Pd onto Colloidal Au Nanorods by Surface Plasmon Excitation. *J. Visualized Exp.* **2019**, *150*, 1−6.

(9) Nafria, R.; Luo, Z.; Ibanez, M.; Marti-Sanchez, S.; Yu, X. T.; de la Mata, M.; Llorca, J.; Arbiol, J.; Kovalenko, M. V.; Grabulosa, A.; Muller, G.; Cabot, A. Growth of Au-Pd2Sn Nanorods via Galvanic Replacement and Their Catalytic Performance on Hydrogenation and Sonogashira Coupling Reactions. *Langmuir* **2018**, *34*, 10634−10643.

(10) Zhou, L.; Liu, Z. K.; Zhang, H.; Cheng, S.; Fan, L. J.; Ma, W. L. Site-specific growth of AgPd nanodendrites on highly purified Au bipyramids with remarkable catalytic performance. *Nanoscale* **2014**, *6*, 12971−12980.

(11) Fei, J. B.; Li, J. B. Controlled Preparation of Porous TiO2-Ag Nanostructures through Supramolecular Assembly for Plasmon-Enhanced Photocatalysis. *Adv. Mater.* **2015**, *27*, 314−319.

(12) He, T. O.; Wang, W. C.; Shi, F. L.; Yang, X. L.; Li, X.; Wu, J. B.; Yin, Y. D.; Jin, M. S. Mastering the surface strain of platinum catalysts for efficient electrocatalysis. *Nature* **2021**, *598*, 76−81.

(13) Hu, Y. X.; Liu, Y. Z.; Li, Z.; Sun, Y. G. Highly Asymmetric, Interfaced Dimers Made of Au Nanoparticles and Bimetallic Nanoshells: Synthesis and Photo-Enhanced Catalysis. *Adv. Funct. Mater.* **2014**, *24*, 2828−2836.

(14) Pan, Y. T.; Qian, Y. Y.; Zheng, X. S.; Chu, S. Q.; Yang, Y. J.; Ding, C. M.; Wang, X.; Yu, S. H.; Jiang, H. L. Precise fabrication of single-atom alloy co-catalyst with optimal charge state for enhanced photocatalysis. *Natl. Sci. Rev.* **2021**, *8*, 224−237.

(15) Xu, L. L.; Cui, Q. Q.; Tian, Y.; Jiao, A. X.; Zhang, M. Y.; Li, S.; Li, H. S.; Chen, M. Enhanced synergistic coupling effect of ternary Au/Ag/AgCl nanochains for promoting natural-solar-driven photocatalysis. *Appl. Surf. Sci.* **2021**, *545*, 149054−149066.

(16) Zhang, H.; Duan, S.; Radjenovic, P. M.; Tian, Z. Q.; Li, J. F. Core-Shell Nanostructure-Enhanced Raman Spectroscopy for Surface Catalysis. *Acc. Chem. Res.* **2020**, *53*, 729−739.

(17) Zhang, Z. L.; Zhang, C. Y.; Zheng, H. R.; Xu, H. X. Plasmon-Driven Catalysis on Molecules and Nanomaterials. *Acc. Chem. Res.* **2019**, *52*, 2506−2515.

(18) Zhou, L. A.; Swearer, D. F.; Zhang, C.; Robatjazi, H.; Zhao, H. Q.; Henderson, L.; Dong, L. L.; Christopher, P.; Carter, E. A.; Nordlander, P.; Halas, N. J. Quantifying hot carrier and thermal contributions in plasmonic photocatalysis. *Science* **2018**, *362*, 69−72.

(19) Mukherjee, S.; Libisch, F.; Large, N.; Neumann, O.; Brown, L. V.; Cheng, J.; Lassiter, J. B.; Carter, E. A.; Nordlander, P.; Halas, N. J. Hot Electrons Do the Impossible: Plasmon-Induced Dissociation of H-2 on Au. *Nano Lett.* **2013**, *13*, 240−247.

(20) Kim, Y.; Wilson, A. J.; Jain, P. K. The Nature of Plasmonically Assisted Hot -Electron Transfer in a Donor-Bridge-Acceptor Complex. *ACS Catal.* **2017**, *7*, 4360−4365.

(21) Guo, J.; Zhang, Y.; Shi, L.; Zhu, Y. F.; Mideksa, M. F.; Hou, K.; Zhao, W. S.; Wang, D. W.; Zhao, M. T.; Zhang, X. F.; Lv, J. W.; Zhang, J. Q.; Wang, X. L.; Tang, Z. Y. Boosting Hot Electrons in Hetero-superstructures for Plasmon-Enhanced Catalysis. *J. Am. Chem. Soc.* **2017**, *139*, 17964−17972.

(22) Xie, W.; Schlucker, S. Hot electron-induced reduction of small molecules on photorecycling metal surfaces. *Nat. Commun.* **2015**, *6*, No. 7570.

(23) Pang, C.; Li, R.; Huang, J. W.; Li, Z. Q.; Chen, M.; Dong, N. N.; Wang, J.; Ren, F.; Chen, F. Ultrafast electron transfer dynamics in Ag/TiO2 nanocomposite for tailoring of optical nonlinearity. *Appl. Surf. Sci.* **2021**, *539*, 148258−148266.

(24) Bai, S. W.; Mei, H.; Huang, W. Z.; Zhang, M. G.; Cheng, L. F. In situ irradiated X-ray photoelectron spectroscopy on Ag-WS2 heterostructure for hydrogen production enhancement. *J. Materiomics* **2021**, *7*, 320−327.

(25) De, S.; Babak, M. V.; Hulsey, M. J.; Ang, W. H.; Yan, N. Designed Precursor for the Controlled Synthesis of Highly Active Atomic and Sub-nanometric Platinum Catalysts on Mesoporous Silica. *Chem. - Asian J.* **2018**, *13*, 1053−1059.

(26) Zuo, Y. P.; Cai, K.; Wu, L.; Li, T. T.; Lv, Z. C.; Liu, J. W.; Shao, K.; Han, H. Y. Spiny-porous platinum nanotubes with enhanced electrocatalytic activity for methanol oxidation. *J. Mater. Chem. A* **2015**, *3*, 1388−1391.

(27) Huang, L.; Wong, P. K.; Tan, J.; Ang, T. P.; Wang, Z. Studies on the Nature of Catalysis: Suppression of the Catalytic Activity of Leached Pd by Supported Pd Particles during the Heck Reaction. *J. Phys. Chem. C* **2009**, *113*, 10120−10130.

(28) Powers, D. C.; Geibel, M. A. L.; Klein, J.; Ritter, T. Bimetallic Palladium Catalysis: Direct Observation of Pd(III)-Pd(III) Intermediates. *J. Am. Chem. Soc.* **2009**, *131*, 17050−17051.

(29) Jain, P. K.; Lee, K. S.; El-Sayed, I. H.; El-Sayed, M. A. Calculated absorption and scattering properties of gold nanoparticles of different size, shape, and composition: Applications in biological imaging and biomedicine. *J. Phys. Chem. B* **2006**, *110*, 7238−7248.

(30) Boerigter, C.; Campana, R.; Morabito, M.; Linic, S. Evidence and implications of direct charge excitation as the dominant mechanism in plasmon-mediated photocatalysis. *Nat. Commun.* **2016**, *7*, No. 10545.

(31) Chen, T.; Tong, F. X.; Enderlein, J.; Zheng, Z. K. Plasmon-Driven Modulation of Reaction Pathways of Individual Pt-Modified Au Nanorods. *Nano Lett.* **2020**, *20*, 3326−3330.

(32) Ding, S. J.; Zhang, H.; Yang, D. J.; Qiu, Y. H.; Nan, F.; Yang, Z. J.; Wang, J. F.; Wang, Q. Q.; Lin, H. Q. Magnetic Plasmon-Enhanced Second-Harmonic Generation on Colloidal Gold Nanocups. *Nano Lett.* **2019**, *19*, 2005−2011.

(33) Ye, R. K.; Zhang, Y. P.; Chen, Y. Y.; Tang, L. F.; Wang, Q.; Wang, Q. Y.; Li, B. S.; Zhou, X.; Liu, J. Y.; Hu, J. Q. Controlling Shape and Plasmon Resonance of Pt-Etched Au@Ag Nanorods. *Langmuir* **2018**, *34*, 5719−5727.

(34) Gil-Negrete, J. M.; Hevia, E. Main group bimetallic partnerships for cooperative catalysis. *Chem. Sci.* **2021**, *12*, 1982−1992.

(35) Ouyang, M.; Papanikolaou, K. G.; Boubnov, A.; Hoffman, A. S.; Giannakakis, G.; Bare, S. R.; Stamatakis, M.; Flytzani-Stephanopoulos, M.; Sykes, E. C. H. Directing reaction pathways via in situ control of active site geometries in PdAu single-atom alloy catalysts. *Nat. Commun.* **2021**, *12*, No. 1549.

(36) Ledesma, B.; Juarez, J.; Mazario, J.; Domine, M.; Beltramone, A. Bimetallic platinum/iridium modified mesoporous catalysts applied in the hydrogenation of HMF. *Catal. Today* **2021**, *360*, 147−156.

(37) Yan, Q.; Wang, X. Y.; Feng, J. J.; Mei, L. P.; Wang, A. J. Simple fabrication of bimetallic platinum-rhodium alloyed nano-multipods: A highly effective and recyclable catalyst for reduction of 4-nitrophenol and rhodamine B. *J. Colloid Interface Sci.* **2021**, *582*, 701−710.

(38) Lyu, Z. H.; Zhu, S. Q.; Xu, L.; Chen, Z. T.; Zhang, Y.; Xie, M. H.; Li, T. H.; Zhou, S.; Liu, J. Y.; Chi, M. F.; Shao, M. H.; Mavrikakis, M.; Xia, Y. N. Kinetically Controlled Synthesis of Pd-Cu Janus Nanocrystals with Enriched Surface Structures and Enhanced Catalytic Activities toward CO2 Reduction. *J. Am. Chem. Soc.* **2021**, *143*, 149−162.

(39) van der Hoeven, J. E. S.; Jelic, J.; Olthof, L. A.; Totarella, G.; van Dijk-Moes, R. J. A.; Krafft, J. M.; Louis, C.; Studt, F.; van Blaaderen, A.; de Jongh, P. E. Unlocking synergy in bimetallic catalysts by core-shell design. *Nat. Mater.* **2021**, *20*, 1216−1220.

(40) Ma, L.; Ding, S. J.; Yang, D. J. Preparation of bimetallic Au/Pt nanotriangles with tunable plasmonic properties and improved photocatalytic activity. *Dalton Trans.* **2018**, *47*, 16969−16976.

(41) Xu, L.; Wang, K.; Jiang, B.; Chen, W.; Liu, F. Y.; Hao, H.; Zou, C.; Yang, Y.; Huang, S. M. Competitive Effect in The Growth of Pd-Au-Pd Segmental Nanorods. *Chem. Mater.* **2016**, *28*, 7394−7403.

(42) Wang, F.; Li, C. H.; Chen, H. J.; Jiang, R. B.; Sun, L. D.; Li, Q.; Wang, J. F.; Yu, J. C.; Yan, C. H. Plasmonic Harvesting of Light Energy for Suzuki Coupling Reactions. *J. Am. Chem. Soc.* **2013**, *135*, 5588−5601.

(43) Jang, H. J.; Hong, S.; Ham, S.; Shuford, K. L.; Park, S. Site-specific growth of a Pt shell on Au nanoplates: tailoring their surface plasmonic behavior. *Nanoscale* **2014**, *6*, 7339−7345.

(44) Deng, T. S.; van der Hoeven, J. E. S.; Yalcin, A. O.; Zandbergen, H. W.; van Huis, M. A.; van Blaaderen, A. Oxidative Etching and Metal Overgrowth of Gold Nanorods within Mesoporous Silica Shells. *Chem. Mater.* **2015**, *27*, 7196−7203.

(45) Yong, Z. J.; Shi, Q. Q.; Fu, R. F.; Cheng, W. L. Fine-Tuning Au@Pd Nanocrystals for Maximum Plasmon-Enhanced Catalysis. *Adv. Mater. Interfaces* **2021**, *8*, No. 2001686.

(46) Chen, S. T.; Reggiano, G.; Thota, S.; Zhao, J. Au-Cu-Ag Nanorods Synthesized by Seed-Mediated Coreduction and Their Optical Properties. *Part. Part. Syst. Charact.* **2017**, *34*, No. 1600384.

(47) Ryu, H. J.; Shin, H.; Oh, S.; Joo, J. H.; Choi, Y.; Lee, J. S. Wrapping AgCl Nanostructures with Trimetallic Nanomeshes for Plasmon-Enhanced Catalysis and in Situ SERS Monitoring of Chemical Reactions. *ACS Appl. Mater. Interfaces* **2020**, *12*, 2842−2853.

(48) Tan, J.; Hussain, S.; Ge, C. X.; Zhan, M. M.; Liu, J. L.; Liu, S. W.; Liu, G. W.; Qiao, G. J. Construction of hierarchical trimetallic organic framework leaf-like nanostructures derived from carbon nanotubes for gas-sensing applications. *J. Hazard. Mater.* **2020**, *400*, No. 123155.

(49) Zhu, C. Z.; Guo, S. J.; Dong, S. J. Facile synthesis of trimetallic AuPtPd alloy nanowires and their catalysis for ethanol electro-oxidation. *J. Mater. Chem.* **2012**, *22*, 14851−14855.

(50) Ahn, J.; Wang, D.; Ding, Y.; Zhang, J. W.; Qin, D. Site-Selective Carving and Co-Deposition: Transformation of Ag Nanocubes into Concave Nanocrystals Encased by Au-Ag Alloy Frames. *ACS Nano* **2018**, *12*, 298−307.

(51) Hagos Gebre, S.; Sendeku, M. G. Trimetallic nanostructures and their applications in electrocatalytic energy conversions. *J. Energy Chem.* **2022**, *65*, 329−352.

(52) Zheng, J. P.; Cheng, X. Z.; Zhang, H.; Bai, X. P.; Ai, R. Q.; Shao, L.; Wang, J. F. Gold Nanorods: The Most Versatile Plasmonic Nanoparticles. *Chem. Rev.* **2021**, *121*, 13342−13453.

(53) Ye, X. C.; Zheng, C.; Chen, J.; Gao, Y. Z.; Murray, C. B. Using Binary Surfactant Mixtures To Simultaneously Improve the Dimensional Tunability and Monodispersity in the Seeded Growth of Gold Nanorods. *Nano Lett.* **2013**, *13*, 765−771.

(54) Wei, M. Z.; Deng, T. S.; Zhang, Q.; Cheng, Z. Q.; Li, S. Q. Seed-Mediated Synthesis of Gold Nanorods at Low Concentrations of CTAB. *ACS Omega* **2021**, *6*, 9188−9195.

(55) Skrabalak, S. E.; Chen, J. Y.; Sun, Y. G.; Lu, X. M.; Au, L.; Cobley, C. M.; Xia, Y. N. Gold Nanocages: Synthesis, Properties, and Applications. *Acc. Chem. Res.* **2008**, *41*, 1587−1595.

(56) Zhang, H.; Jin, M. S.; Liu, H. Y.; Wang, J. G.; Kim, M. J.; Yang, D. R.; Xie, Z. X.; Liu, J. Y.; Xia, Y. N. Facile Synthesis of Pd-Pt Alloy Nanocages and Their Enhanced Performance for Preferential Oxidation of CO in Excess Hydrogen. *ACS Nano* **2011**, *5*, 8212−8222.

(57) Huang, X. Q.; Zhang, H. H.; Guo, C. Y.; Zhou, Z. Y.; Zheng, N. F. Simplifying the Creation of Hollow Metallic Nanostructures: One-Pot Synthesis of Hollow Palladium/Platinum Single-Crystalline Nanocubes. *Angew. Chem., Int. Ed.* **2009**, *48*, 4808−4812.

(58) Moreau, L. M.; Schurman, C. A.; Kewalramani, S.; Shahjamali, M. M.; Mirkin, C. A.; Bedzyk, M. J. How Ag Nanospheres Are Transformed into AgAu Nanocages. *J. Am. Chem. Soc.* **2017**, *139*, 12291−12298.

(59) Liu, H. P.; Liu, K.; Zhong, P.; Qi, J.; Bian, J. H.; Fan, Q. K.; Ren, K.; Zheng, H. Q.; Han, L.; Yin, Y. D.; Gao, C. B. Ultrathin Pt-Ag Alloy Nanotubes with Regular Nanopores for Enhanced Electrocatalytic Activity. *Chem. Mater.* **2018**, *30*, 7744−7751.

(60) Xie, F.; Ye, W.; Sun, H. Y.; Kou, S. F.; Guo, X. Silver Ions Induce Lateral Etching of Gold Nanorods by K_2PtCl_4. *Langmuir* **2015**, *31*, 6823−6828.

(61) Oksenberg, E.; Shlesinger, I.; Xomalis, A.; Baldi, A.; Baumberg, J. J.; Koenderink, A. F.; Garnett, E. C. Energy-resolved plasmonic chemistry in individual nanoreactors. *Nat. Nanotechnol.* **2021**, *16*, 1378−1385.

(62) Forcherio, G. T.; Baker, D. R.; Boltersdorf, J.; Leff, A. C.; McClure, J. P.; Grew, K. N.; Lundgren, C. A. Targeted Deposition of Platinum onto Gold Nanorods by Plasmonic Hot Electrons. *J. Phys. Chem. C* **2018**, *122*, 28901−28909.

(63) Sarina, S.; Bai, S.; Huang, Y. M.; Chen, C.; Jia, J. F.; Jaatinen, E.; Ayoko, G. A.; Bao, Z.; Zhu, H. Y. Visible light enhanced oxidant

free dehydrogenation of aromatic alcohols using Au-Pd alloy nanoparticle catalysts. *Green Chem.* **2014**, *16*, 331−341.

(64) Baffou, G.; Quidant, R.; Girard, C. Heat generation in plasmonic nanostructures: Influence of morphology. *Appl. Phys. Lett.* **2009**, *94*, No. 153109.

(65) Palik, E. E. D.*Handbook of Optical Constants of Solids*; Academic Press, 1991.

(66) Werner, W. S. M.; Glantschnig, K.; Ambrosch-Draxl, C. Optical Constants and Inelastic Electron-Scattering Data for 17 Elemental Metals. *J. Phys. Chem. Ref. Data* **2009**, *38*, 1013−1092.

(67) Garnet, J. C. M. XII Colours in Metal Glasses and in Metallic Films. *Philos. Trans. R. Soc., A* **1904**, *203*, 385−420.

https://doi.org/10.1021/acsanm.2c03953
ACS Appl. Nano Mater. 2022, 5, 17048−17058

Supporting Information

Trimetallic Nanostructures of Silver-Platinum Alloy Shells on Gold Nanorods for Plasmon-Mediated Photocatalysis

Qi Zhang[†], *Tian-Song Deng*[†,*], *Yun-Qi Dou*[†], *Ming-Zhang Wei*[†], *Shiqi Li*[†], *Jia Liu*[‡], *and Zhiqun Cheng*[†]

[†]School of Electronics and Information Engineering, Hangzhou Dianzi University, Hangzhou 310018, P. R. China.

[‡]College of Materials and Environmental Engineering, Hangzhou Dianzi University, Hangzhou 310018, P. R. China.

* *Corresponding author. E-mail: dengts@pku.edu.cn*

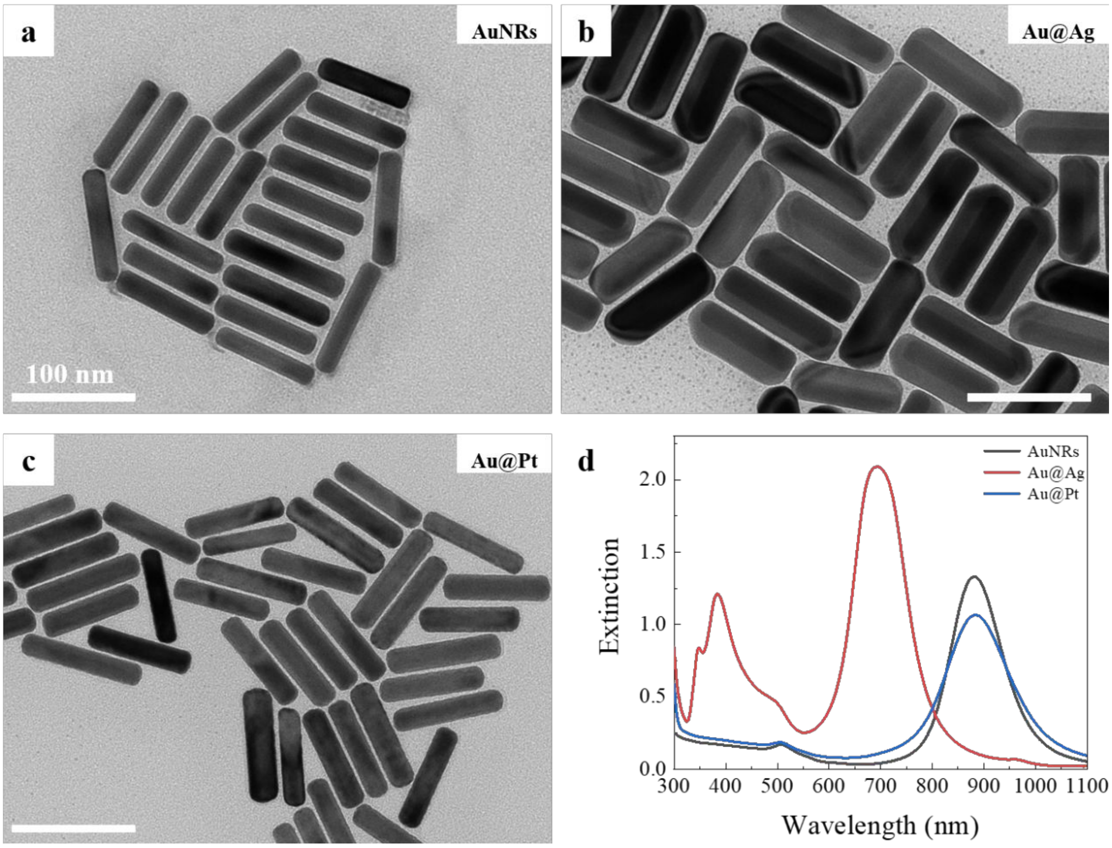

Figure S1. TEM images and UV-vis-NIR spectra of nanoparticles. TEM images of (a) AuNRs, (b) Au@Ag NRs, and (c) Au@Pt NRs. Scale bar is 100 nm. (d) UV-vis-NIR spectra of the AuNRs (black), Au@Ag NRs (red), and Au@Pt NRs (blue). The AuNRs samples are 88.7 ± 7.0 nm in length and 17.1 ± 1.7 nm in width. The Au@Ag samples are core-shell cuboid structures with size of 98.8 ± 5.9 nm in length and 33.8 ± 2.0 nm in width, while Au@Pt samples with 88.1 ± 5.6 nm in length and 19.1± 1.6 nm in width. It should be noted that the Ag overgrowth was asymmetric since the reaction rate is too fast when 0.20 mL $AgNO_3$ was added.

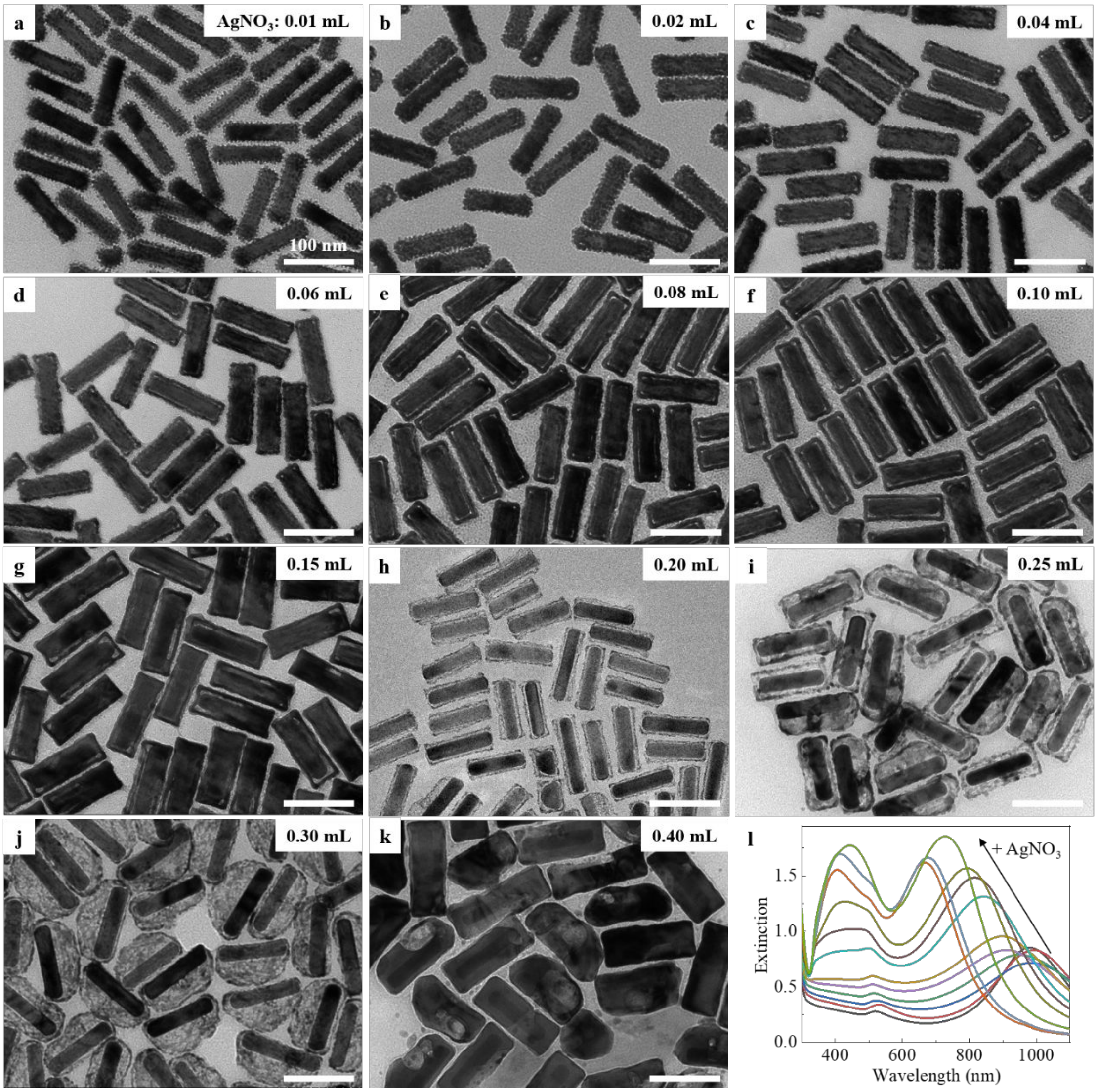

Figure S2. TEM and UV-vis-NIR spectra analysis of nanoparticles. The TEM images of Au@AgPt with different amount of AgNO$_3$, (a) 0.01 mL, (b) 0.02 mL, (c) 0.04 mL, (d) 0.06 mL, (e) 0.08 mL, (f) 0.10 mL, (g) 0.15 mL, (h) 0.20 mL, (i) 0.25 mL, (j) 0.30 mL, and (k) 0.40 mL. Scale bar is 100 nm. The morphology of the Au@AgPt changes from heterostructure, to hollow alloy shell., and then to asymmetric core-shell structure. (l) UV-vis-NIR spectra of the Au@AgPt with different AgNO$_3$ from 0.01 mL to 0.40 mL. With the increase of AgNO$_3$, the LSPRs gradually blue-shifted, and the intensity increased. The arrow direction indicates the increasing amount of AgNO$_3$.

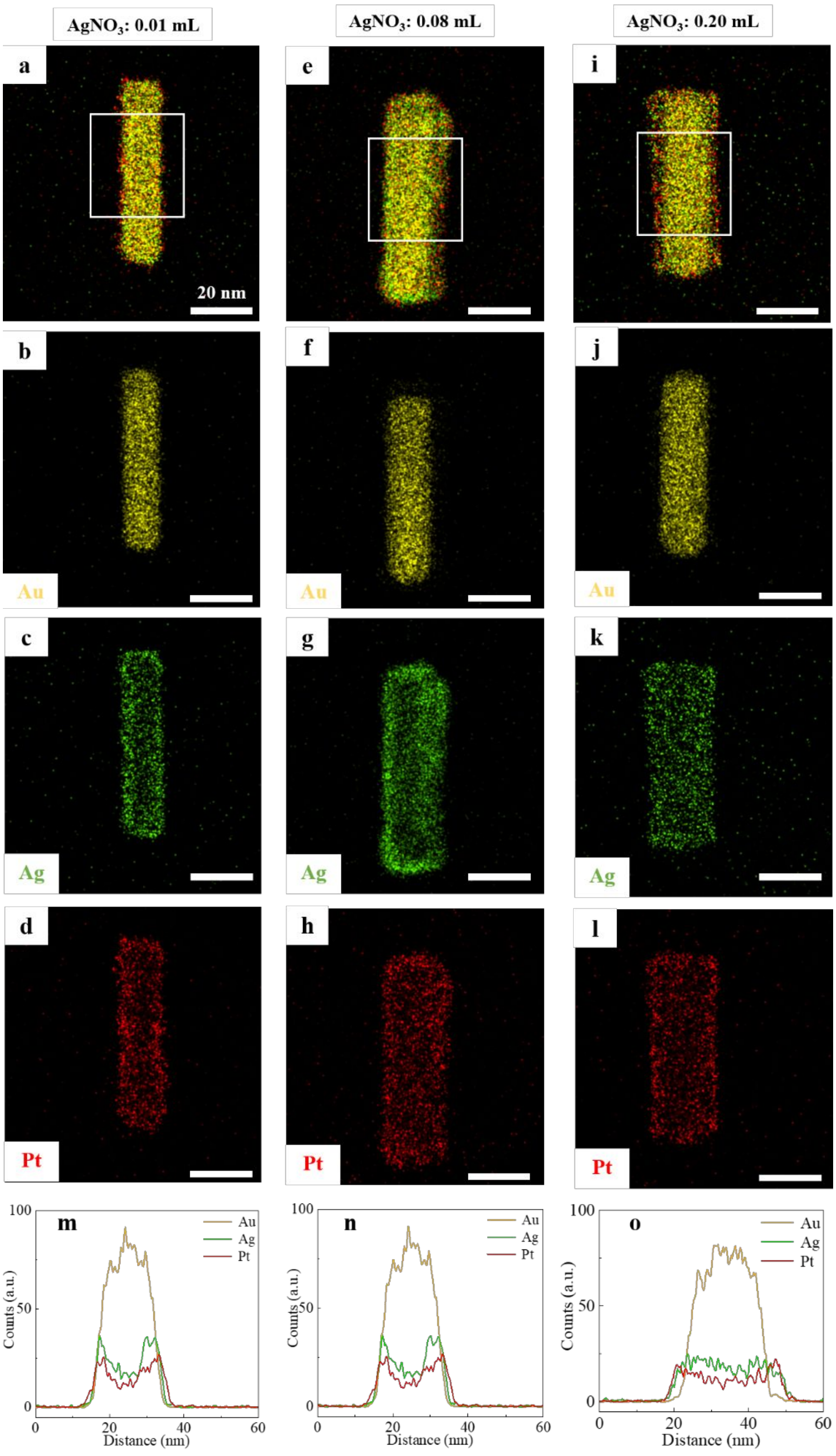

N

Figure S3. EDS mapping of Au@AgPt nanostructures. (a) EDS mapping of a single Au@AgPt with 0.01 mL AgNO$_3$. (b)-(d) element of Au (b), Ag (c), and Pt (d) in Au@AgPt nanostructure, respectively; (e) EDS mapping of a single Au@AgPt with 0.08 mL AgNO$_3$. (f)-(h) element of Au (f), Ag (g), and Pt (h) in Au@AgPt nanostructure; (i) EDS mapping of a single Au@AgPt nanoparticle with 0.20 mL AgNO$_3$. (j)-(l) element of Au (j), Ag (k), and Pt (l) in Au@AgPt nanostructure. All scales bars are 20 nm. Elemental distribution of Au (yellow), Ag (green), Pt (red) in EDS mapping (first row) of samples with (m) 0.01 mL, (n) 0.08 mL, (o) 0.20 mL of AgNO$_3$.

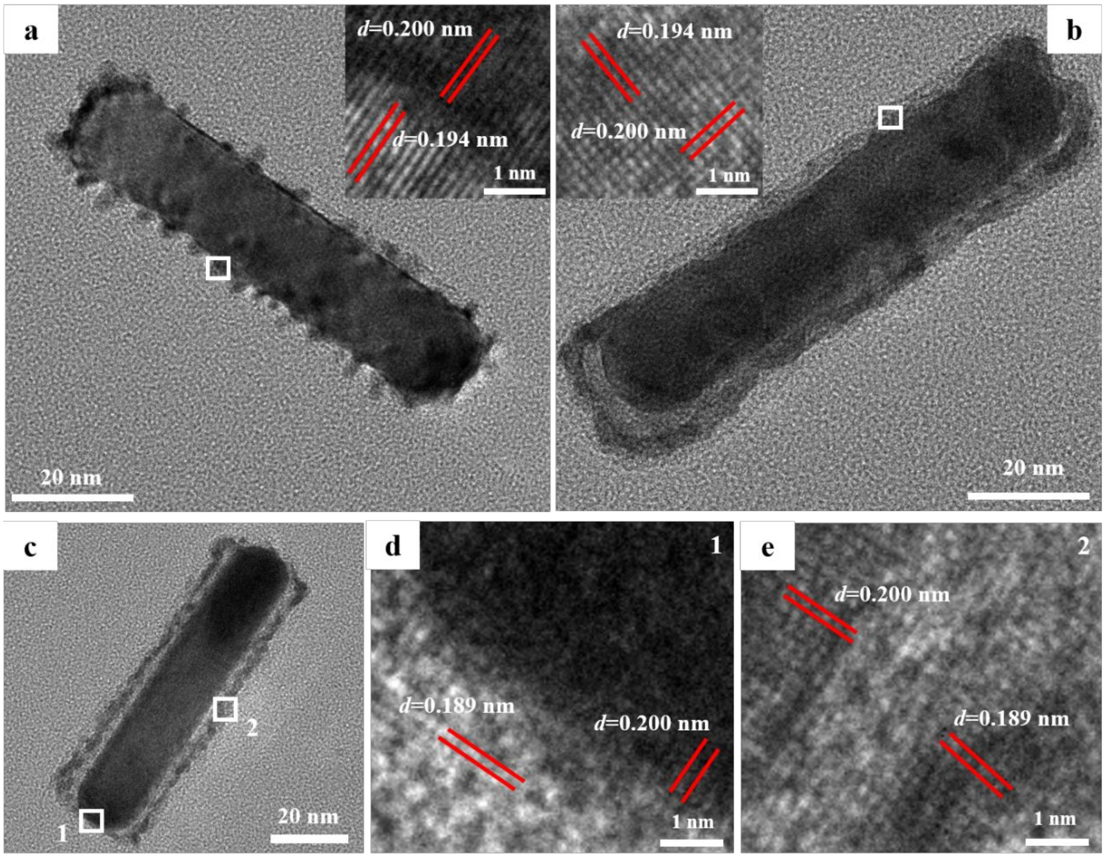

Figure S4. HRTEM analysis of Au@AgPt nanostructures. (a) TEM image of a single Au@AgPt with different amount of $AgNO_3$ (a) 0.01 mL, (the insert image is the HRTEM of the white square area). (b) 0.08 mL (the insert image is the HRTEM of the white square area). The crystal plane spacing of 0.200 nm is a family of Au {200} facets, and the spacing of 0.194 nm is the Pt {200} facets. (c) 0.20 mL. TEM image of a single Au@AgPt hollow alloy shell. HRTEM images of regions 1 and 2 are shown in (d) and (e). The crystal plane spacing of 0.200 nm is a family of Au {200} facets, and the spacing of 0.189 nm is the AgPt {200} facets.

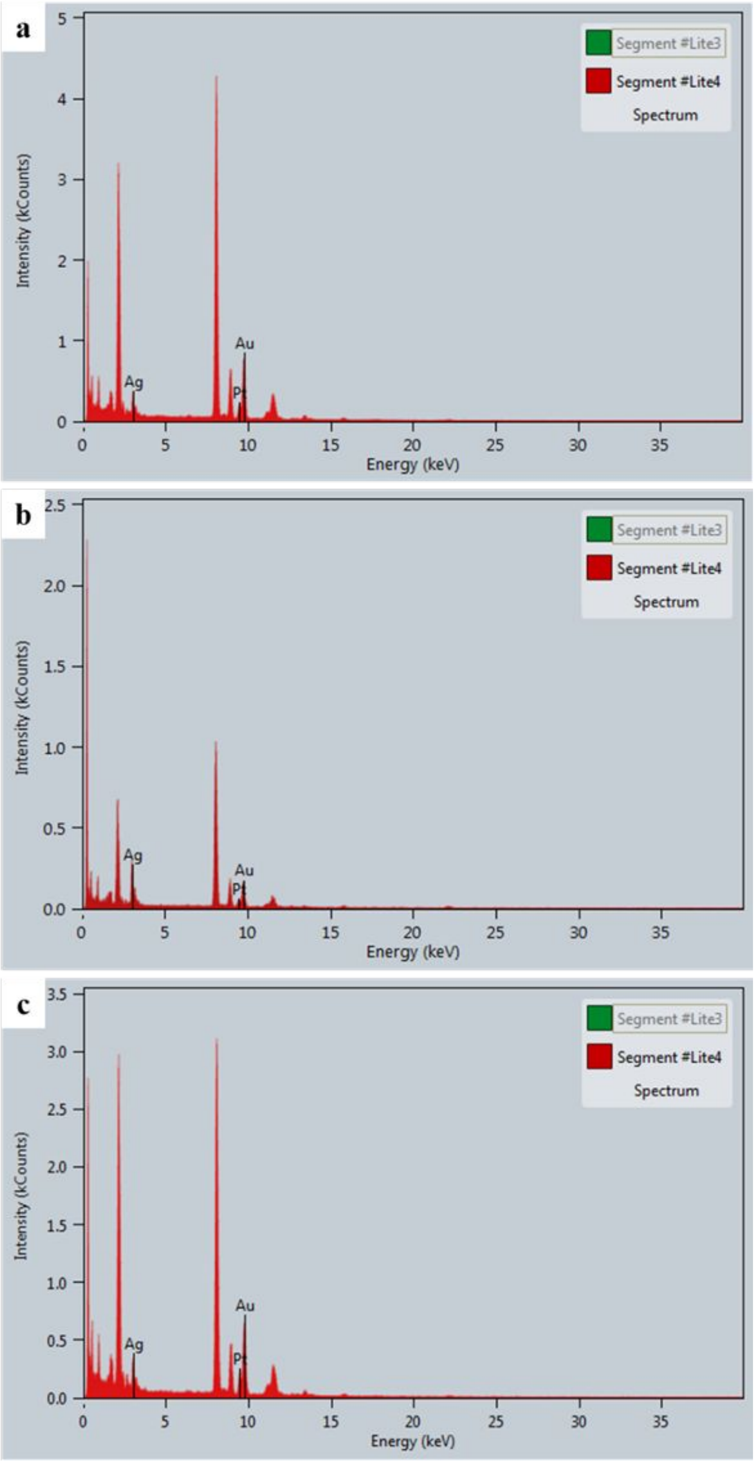

Figure S5. Net counts of Au, Ag and Pt in tri-metal nanostructures with (a) 0.01 mL, (b) 0.08 mL, and (c) 0.20 mL $AgNO_3$. And the atomic ratio of Au, Ag, and Pt is 61.64%, 21.44% and 16.92% in (a), 38.51%, 47.65%, and 13.85% in (b), 57.57%, 24.13% and 18.31% in (c), respectively.

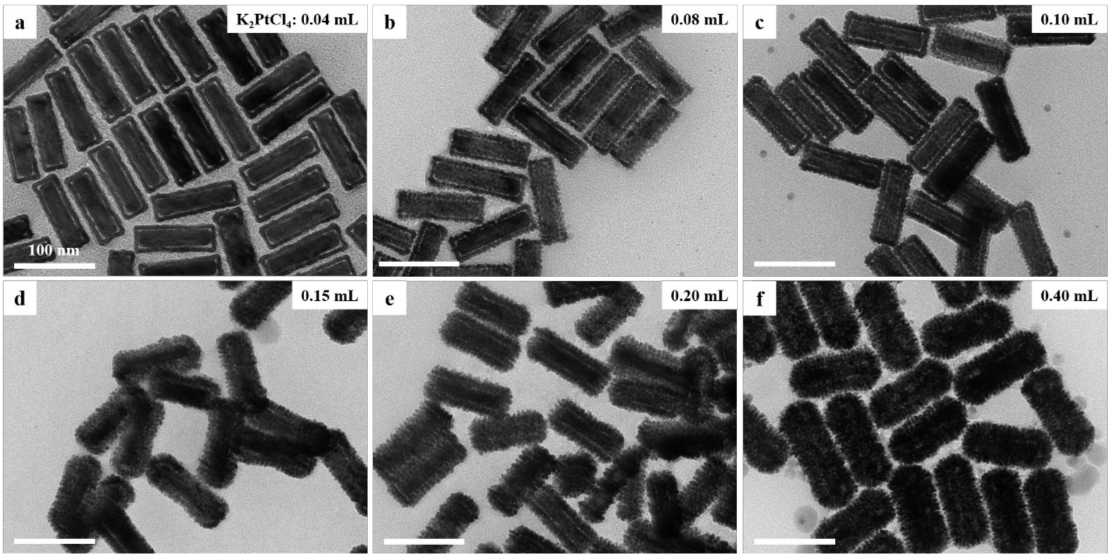

Figure S6. TEM images of nanoparticles with different K_2PtCl_4 (a) 0.04 mL, (b) 0.08 mL, (c) 0.10 mL, (d) 0.15 mL, (e) 0.20 mL, and (f) 0.40 mL K_2PtCl_4. the morphology of the nanoparticles changes from alloy shell to dendritic structures.

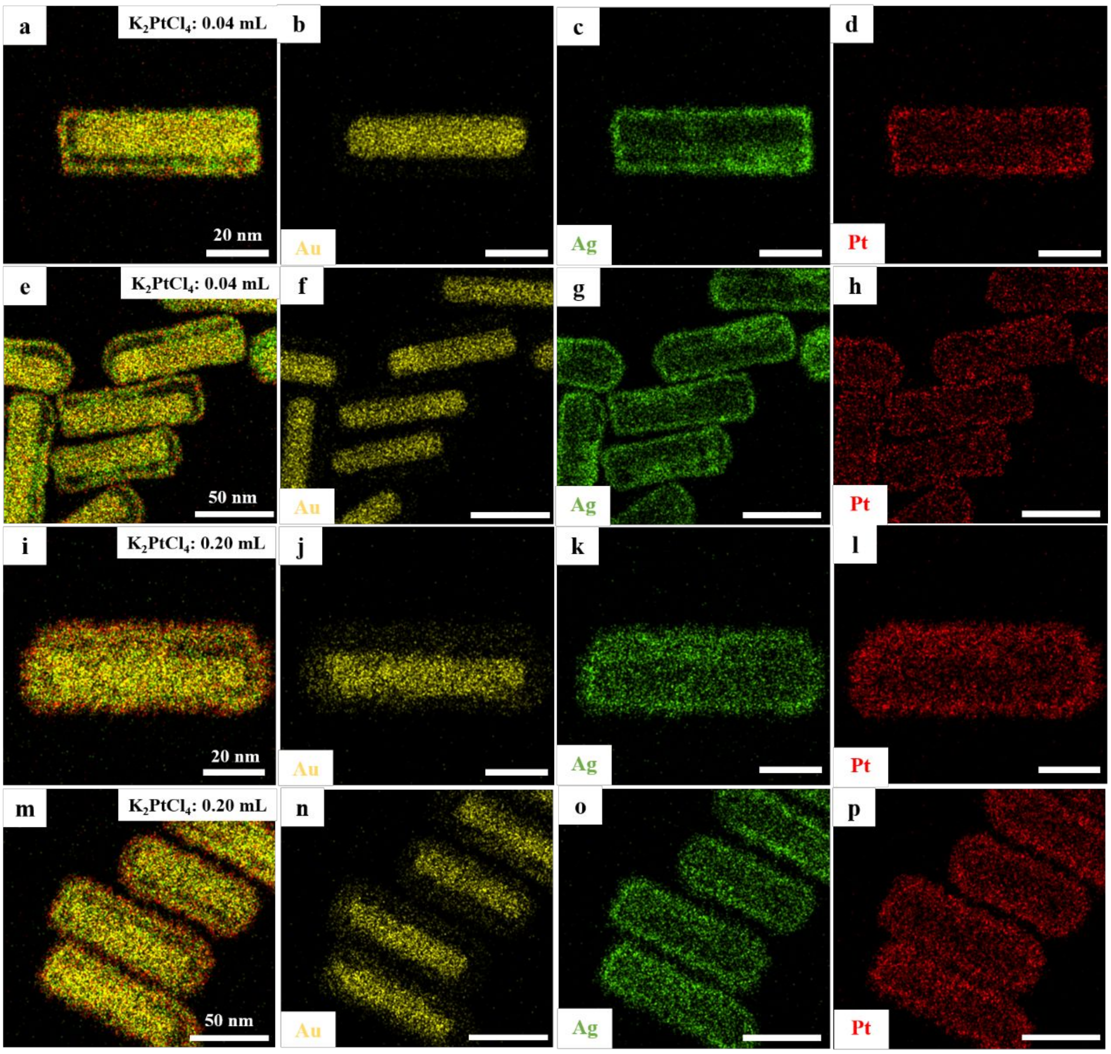

Figure S7. EDS mapping of Au@AgPt nanostructures with different amount of K_2PtCl_4. (a) EDS mapping of the single Au@AgPt nanoparticle with 0.04 mL K_2PtCl_4. (b) element of Au in Au@AgPt nanostructure (yellow), (c) element of Ag in Au@AgPt nanostructure (green), (d) element of Pt in Au@AgPt nanostructure (red), respectively; (e) EDS mapping of some Au@AgPt nanoparticles with 0.04 mL K_2PtCl_4. (f) element of Au in Au@AgPt nanostructure (yellow), (g) element of Ag in Au@AgPt nanostructure (green), (h) element of Pt in Au@AgPt nanostructure (red), respectively; Scale bar is 50 nm. (i) EDS mapping of the single Au@AgPt nanoparticle with 0.20 mL K_2PtCl_4. (j) element of Au in Au@AgPt nanostructure (yellow), (k) element of Ag in Au@AgPt nanostructure (green), (l) element of Pt in Au@AgPt nanostructure (red), respectively; scale bar is 20 nm. (m) EDS mapping of some Au@AgPt nanoparticles with 0.20 mL K_2PtCl_4. (n) element of Au in Au@AgPt nanostructure (yellow), (o) element of Ag in Au@AgPt nanostructure (green), (p) element of Pt in Au@AgPt nanostructure (red), respectively; Scale bar is 50 nm.

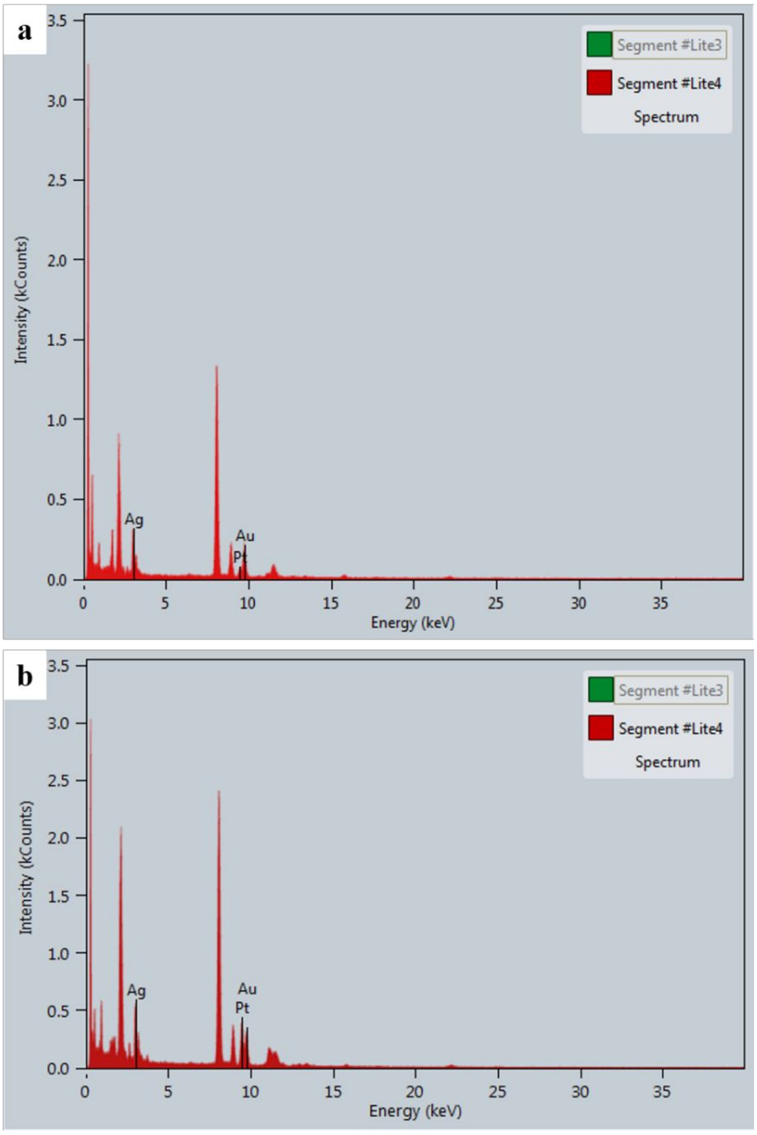

Figure S8. Net counts of Au, Ag and Pt in tri-metal nanostructures with (a) 0.04 mL, (b) 0.2 mL K_2PtCl_4. And the atomic ratio of Au, Ag, and Pt is 40.61%, 45.51%, 13.88% in (a), and 29.40%, 36.27%, 34.33% in (b), respectively.

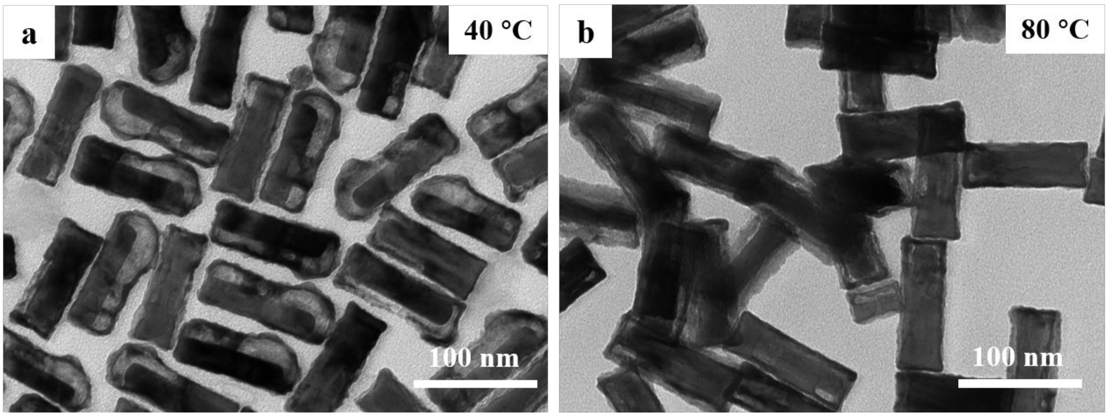

Figure S9. Effects of reaction temperature on Au@AgPt synthesis. TEM images of Au@AgPt in (a) 40 °C, and (b) 80 °C. The Au@AgPt nanostructures synthesized at 40 °C are not uniform, while at 80 °C have few hollow nanostructures.

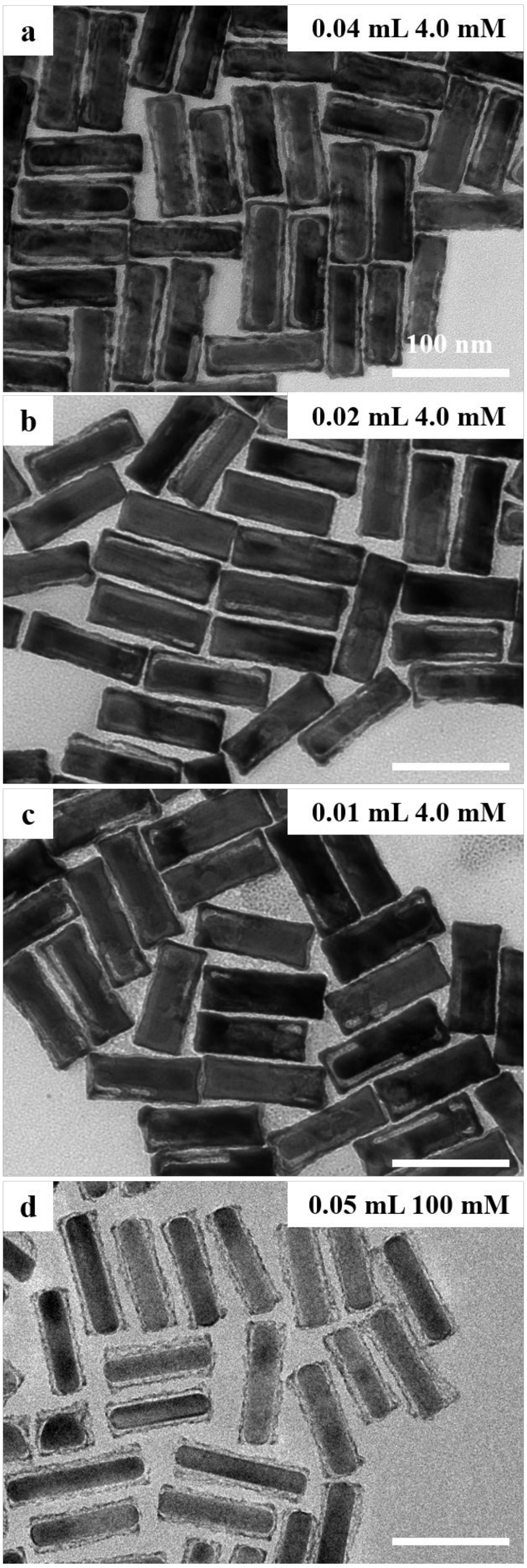

Figure S10. Effects of ascorbic acid on Au@AgPt synthesis. (a) 0.04 mL 4.0 mM, (b) 0.02 mL 4.0 mM, (c) 0.01 mL 4.0 mM, (d) 0.05 mL 100 mM. When less amount of AA was used, the Au@AgPt with incomplete hollow nanostructure were obtained.

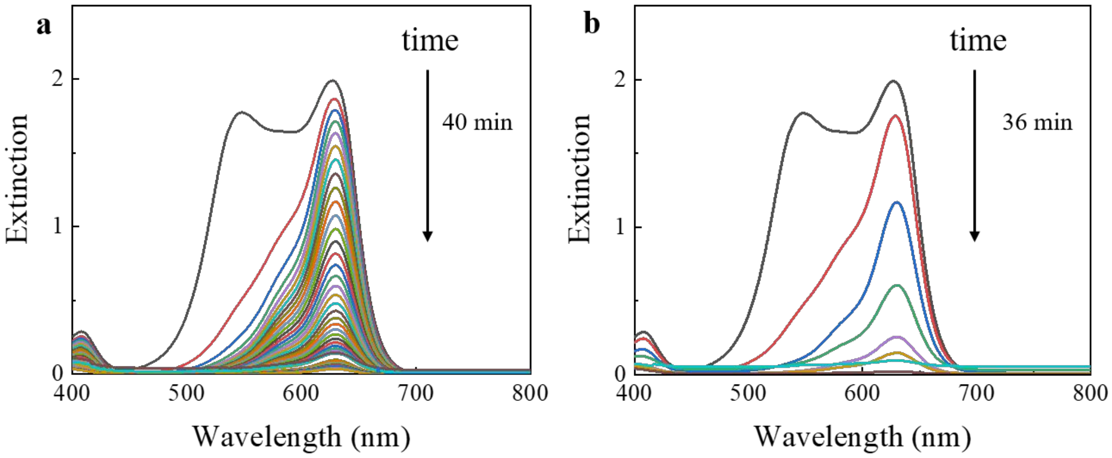

Figure S11. vis-NIR spectra of MB reduction process. Arrow directions indicate changes of the spectrum over time. (a) Extinction spectra of MB reduced by $NaBH_4$ under dark environment. The entire reaction was recorded at one-minute intervals, and the reduced time is 40 minutes. (b) Extinction spectra of MB reduced by $NaBH_4$ under light irradiation. The entire reaction was recorded at six-minutes intervals, the reduced time is 36 minutes.

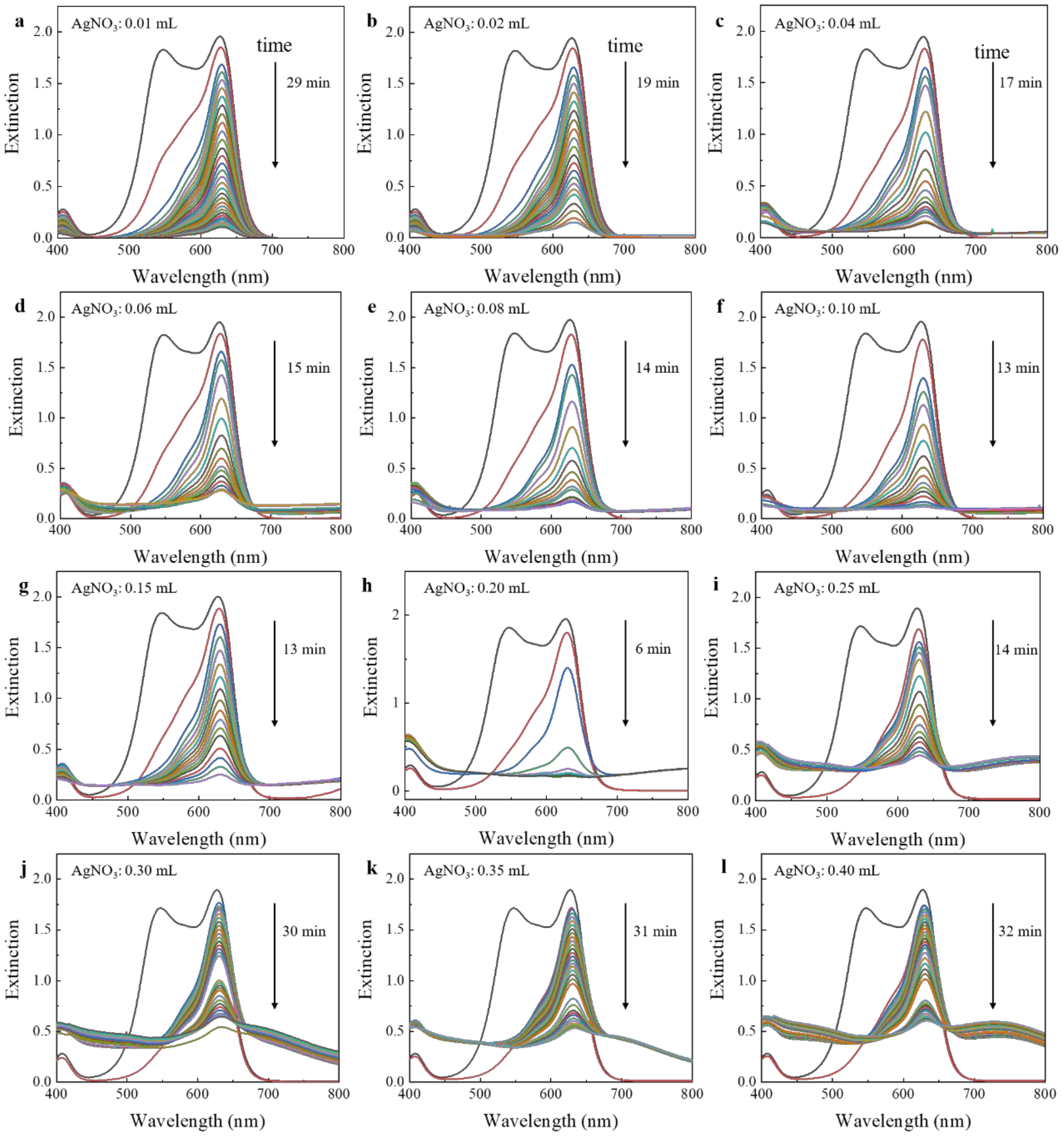

Figure S12. Vis-NIR spectra of Au@AgPt with different amount of AgNO$_3$ under the dark environment, the arrow shows the variation of the spectrum over time. (a) 0.01 mL, (b) 0.02 mL, (c) 0.04 mL, (d) 0.06 mL, (e) 0.08 mL, (f) 0.10 mL, (g) 0.15 mL, (h) 0.20 mL, (i) 0.25 mL, (j) 0.30 mL, (k) 0.35 mL, (l) 0.40 mL, respectively. And the reaction time are 29 min, 19 min, 17 min, 15 min, 14 min, 13 min, 13 min, 6 min, 14 min, 30 min, 31 min, 32 min, respectively.

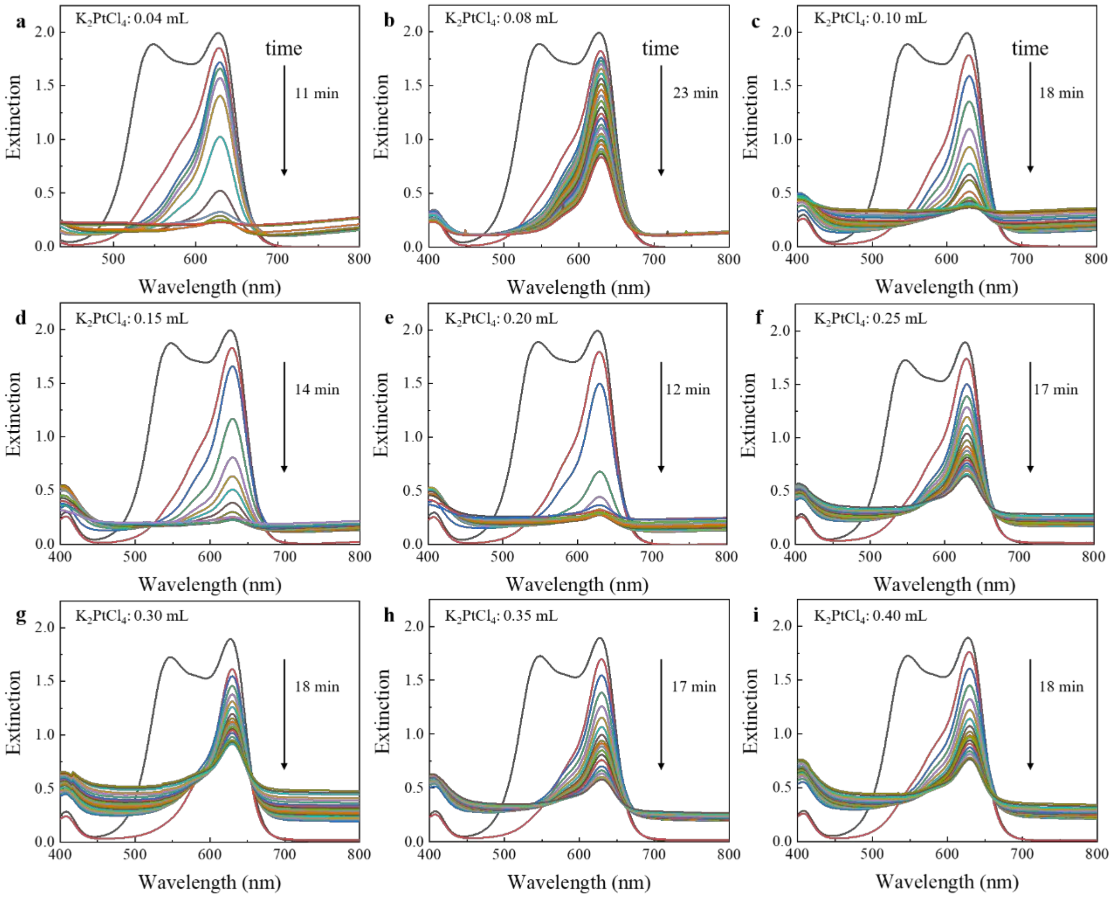

Figure S13. Vis-NIR spectra of Au@AgPt with different amount of K_2PtCl_4 under the dark environment, the arrow shows the variation of the spectrum over the time. (a) 0.04 mL K_2PtCl_4, (b) 0.08 mL K_2PtCl_4, (c) 0.10 mL K_2PtCl_4, (d) 0.15 mL K_2PtCl_4, (e) 0.20 mL K_2PtCl_4, (f) 0.25 mL K_2PtCl_4, (g) 0.30 mL K_2PtCl_4, (h) 0.35 mL K_2PtCl_4, (i) 0.40 mL K_2PtCl_4. The reaction time are 11 min, 23 min, 18 min, 14 min, 12 min, 17 min, 18 min, 17 min, 18 min, respectively.

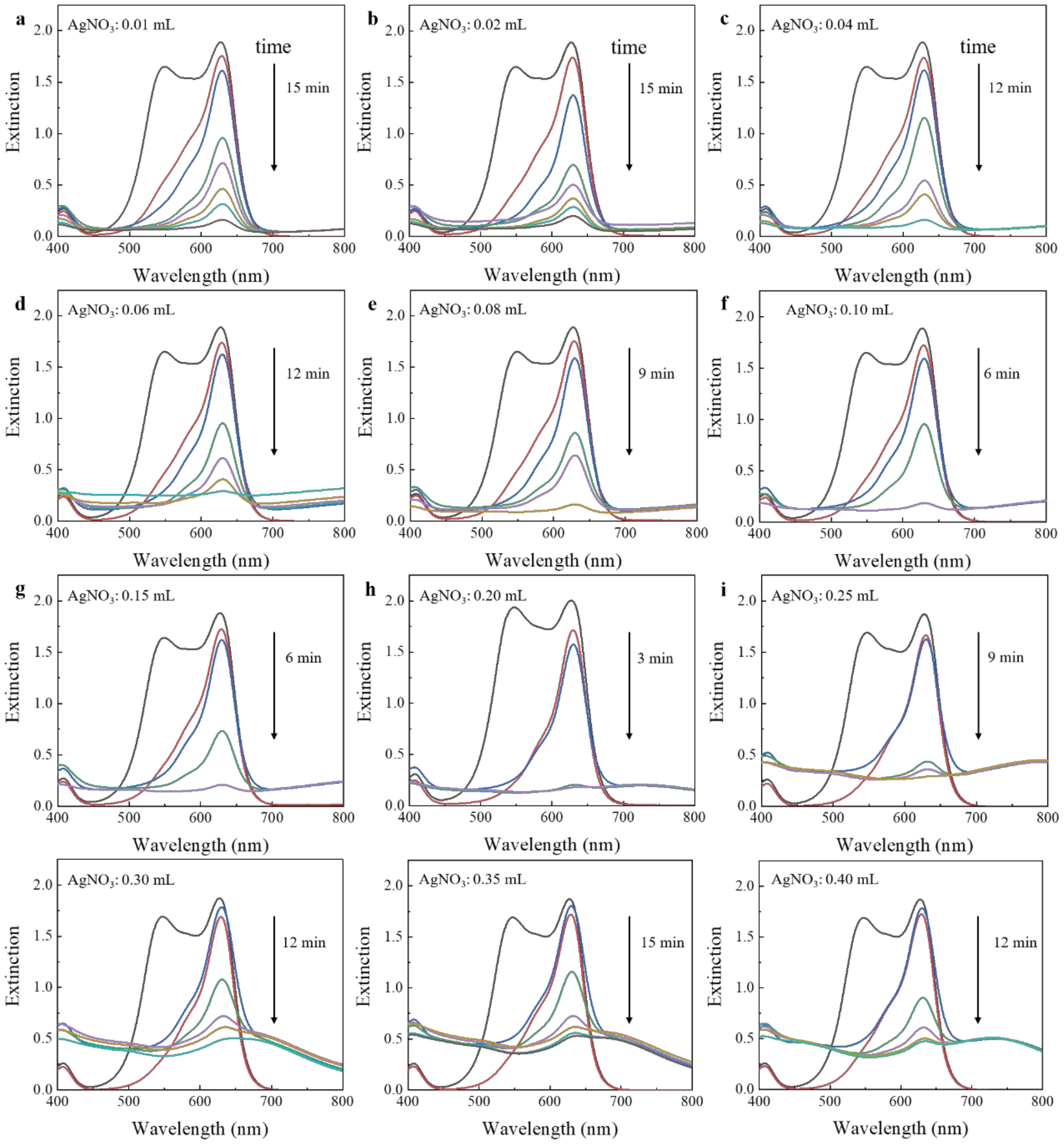

Figure S14. Vis-NIR spectra of Au@AgPt with different amount of AgNO$_3$ under light irradiation, the arrow shows the variation of the spectrum over the time. (a) 0.01 mL AgNO$_3$, (b) 0.02 mL AgNO$_3$, (c) 0.04 mL AgNO$_3$, (d) 0.06 mL AgNO$_3$, (e) 0.08 mL AgNO$_3$, (f) 0.10 mL AgNO$_3$, (g) 0.15 mL AgNO$_3$, (h) 0.20 mL AgNO$_3$, (i) 0.25 mL AgNO$_3$, (j) 0.30 mL AgNO$_3$, (k) 0.35 mL AgNO$_3$, (l) 0.40 mL AgNO$_3$. The reaction time are 15 min, 15 min, 12 min, 12 min, 9 min, 6 min, 6 min, 3 min, 9 min, 12 min, 15 min, 12 min, respectively. Under the light irradiation, the sample with 0.20 mL AgNO$_3$ as the photocatalyst has the best photocatalytic efficiency.

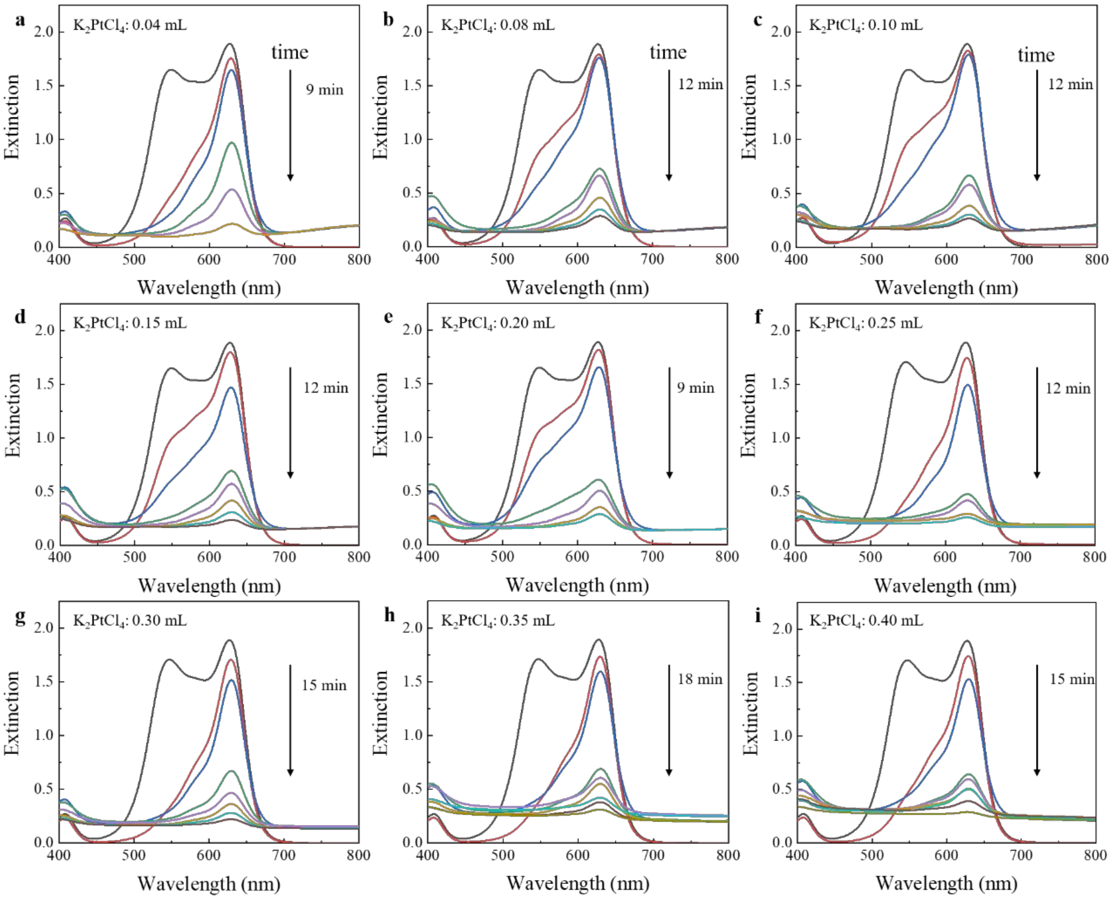

Figure S15. Vis-NIR spectra of Au@AgPt with different amount of K_2PtCl_4 under light irradiation, the arrow shows the variation of the spectrum over the time. (a) 0.04 mL K_2PtCl_4, (b) 0.08 mL K_2PtCl_4, (c) 0.10 mL K_2PtCl_4, (d) 0.15 mL K_2PtCl_4, (e) 0.20 mL K_2PtCl_4, (f) 0.25 mL K_2PtCl_4, (g) 0.30 mL K_2PtCl_4, (h) 0.35 mL K_2PtCl_4, (i) 0.40 mL K_2PtCl_4, the reaction time are 9 min, 12 min, 12 min, 12 min, 9 min, 12 min, 15 min, 18 min, 15 min, respectively.

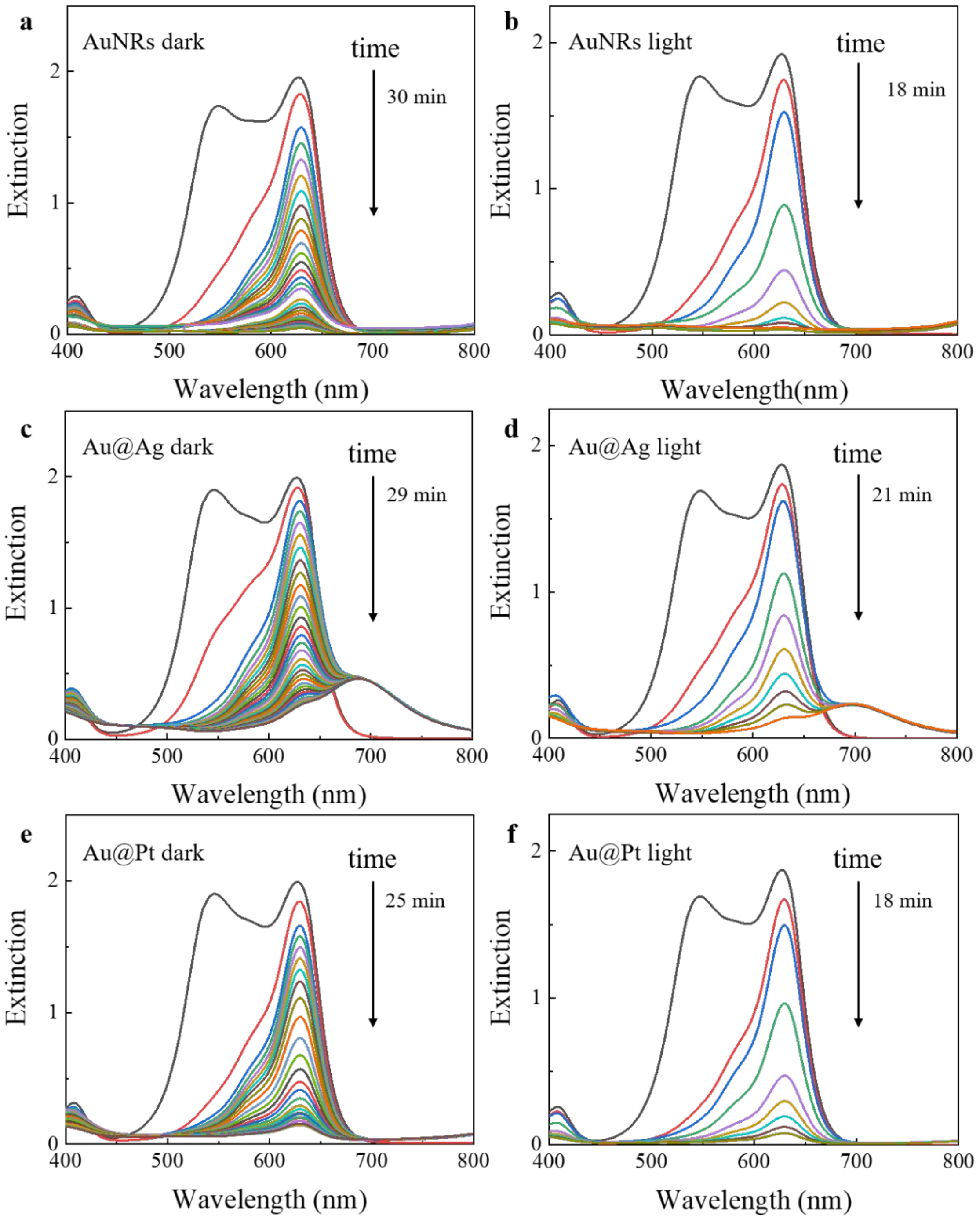

Figure S16. Vis-NIR spectra of MB reduced by different catalysts. The spectra of MB reduced by $NaBH_4$ under (a) AuNRs (c) Au@Ag, (e) Au@Pt catalyzing in dark environment. The entire reaction was recorded at one-minute intervals, and the reduced time are 30 minutes, 29 minutes and 25 minutes, respectively. The spectra of MB reduced by $NaBH_4$ under (b) AuNRs, (d) Au@Ag, (f) Au@Pt catalyzing in light irradiation. The entire reaction was recorded at three-minutes intervals, and the time are 18 minutes, 21 minutes and 18 minutes, respectively.

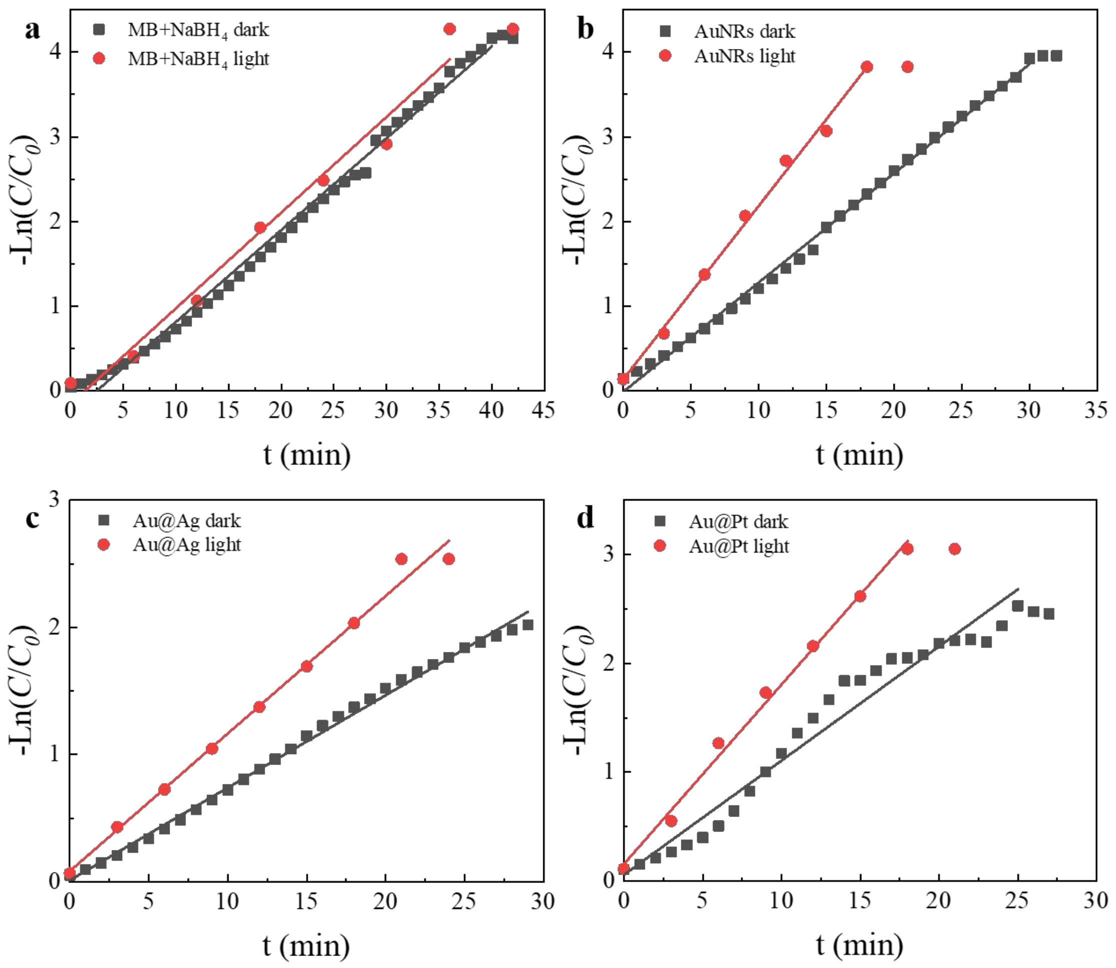

Figure S17. Reaction rates of catalytic process by linear fitting. (a) The rate fitting of MB/NaBH$_4$ in dark (black) and light condition (red). (b) The reduction of MB by NaBH$_4$ was catalyzed by AuNRs in dark (black) and light condition (red). (c) The reduction of MB by NaBH$_4$ was catalyzed by Au@Ag bimetallic nanostructures in dark (black) and light condition (red). (d) The reduction of MB by NaBH$_4$ was catalyzed by Au@Pt bimetallic nanostructures in dark (black) and light condition (red).

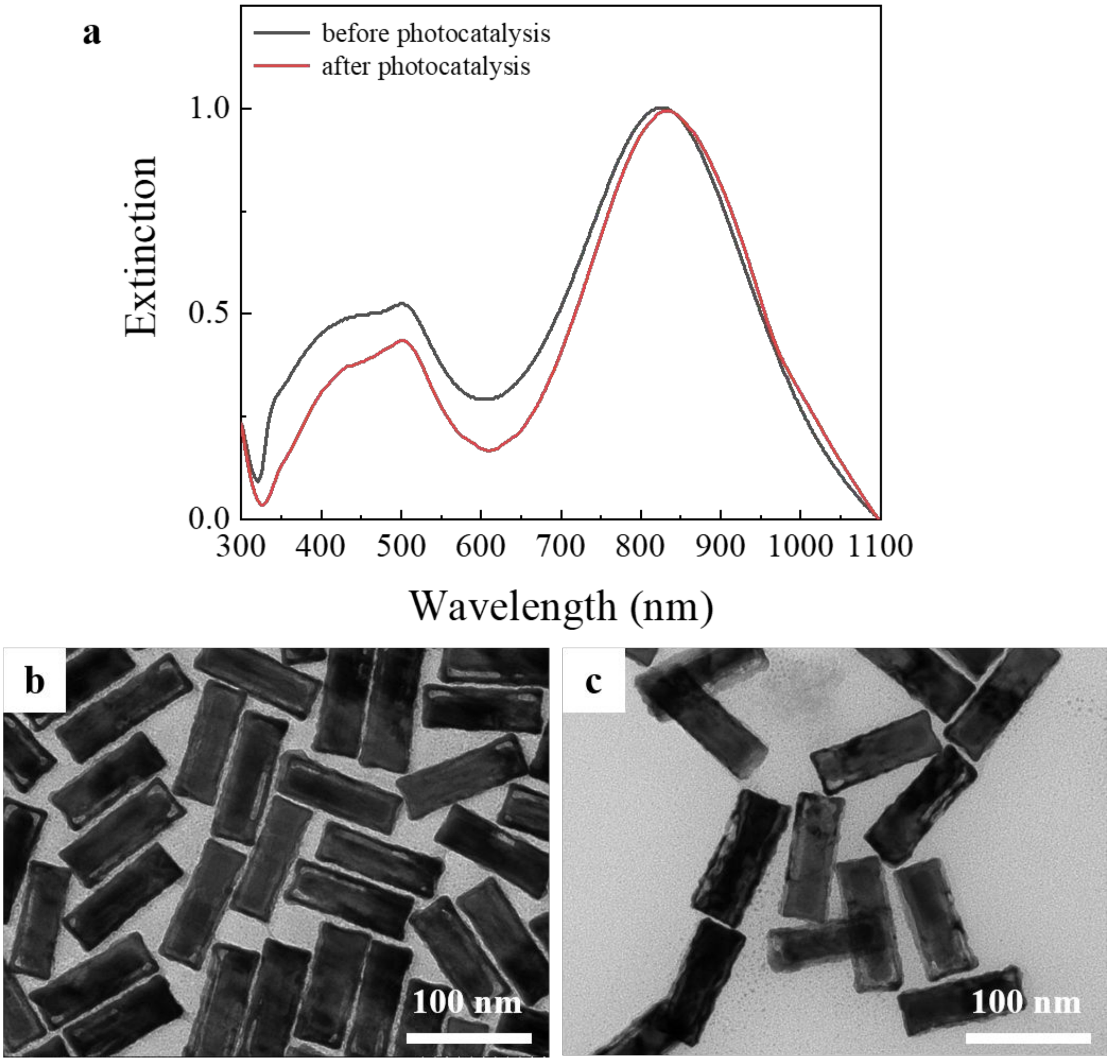

Figure S18. Cyclic characteristic test. (a) Normalized UV-vis-NIR spectra of MB reduced by NaBH$_4$ with Au@AgPt catalysts under light irradiation. (b, c) TEM images of Au@AgPt before photocatalysis (b), and after ten photocatalytic cycles (c).

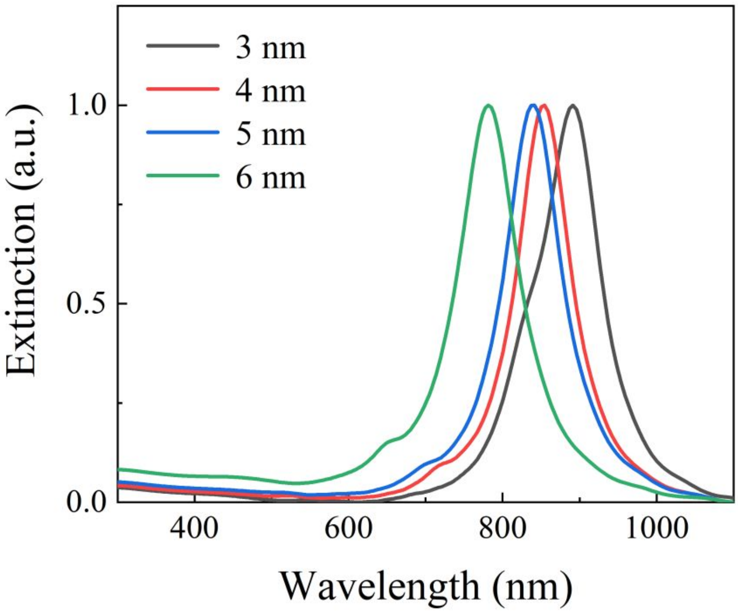

Figure S19. FDTD simulation of Au@AgPt HAS nanostructures with different AgPt alloy shell thickness (3-6 nm). The LSPR blue-shifted with increase of the AgPt shell thickness.

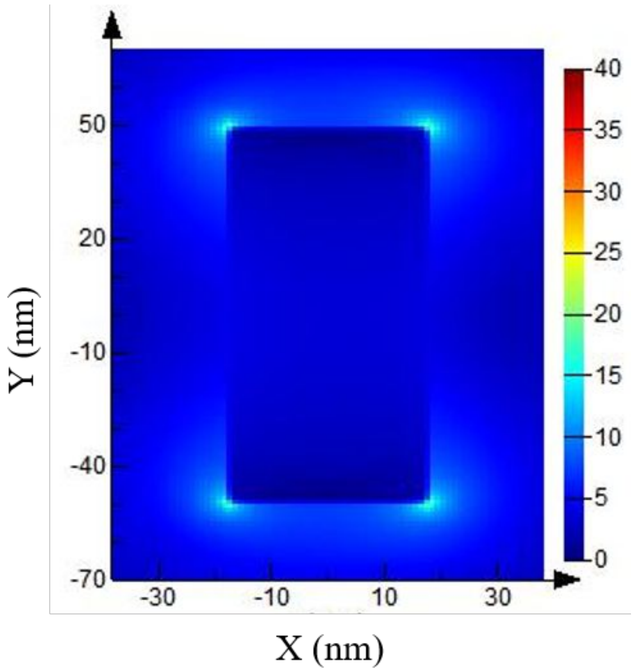

Figure S20. Electric field distribution of a single Au@AgPt solid structure by FDTD simulation, the hot spots are located in the four vertices of AgPt outer layer, and the intensity is much weaker than that of the Au@AgPt hollow alloy shell nanostructures (Fig. 5b).

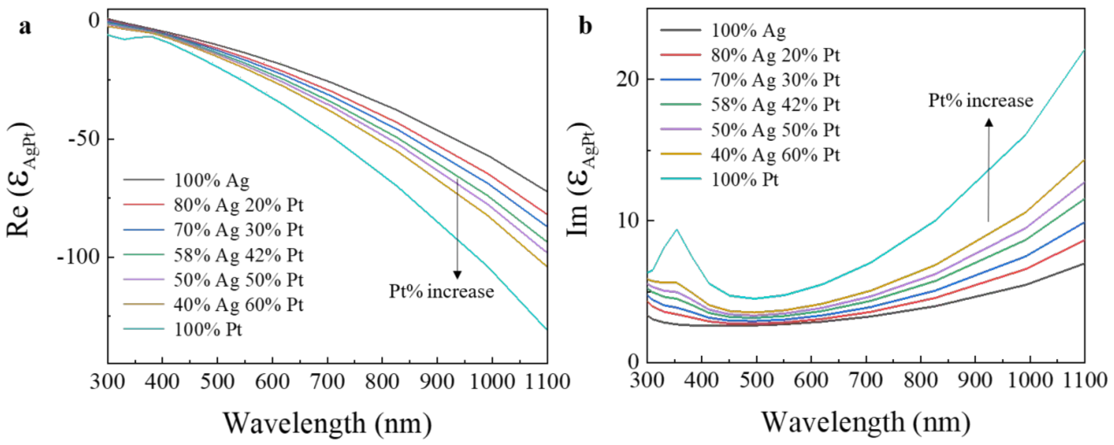

Figure S21. Dielectric function of AgPt alloy with different Ag/Pt ratio. (a) is the real part and (b) is the imaginary part. The arrow shows the direction of increasing Pt%. With the increase of Pt%, both absolute values of the real part and the imaginary part of dielectric functions of the AgPt alloy increased. Note that 58%Ag42%Pt (obtained from EDS mapping) was used in the manuscript for FDTD simulations.

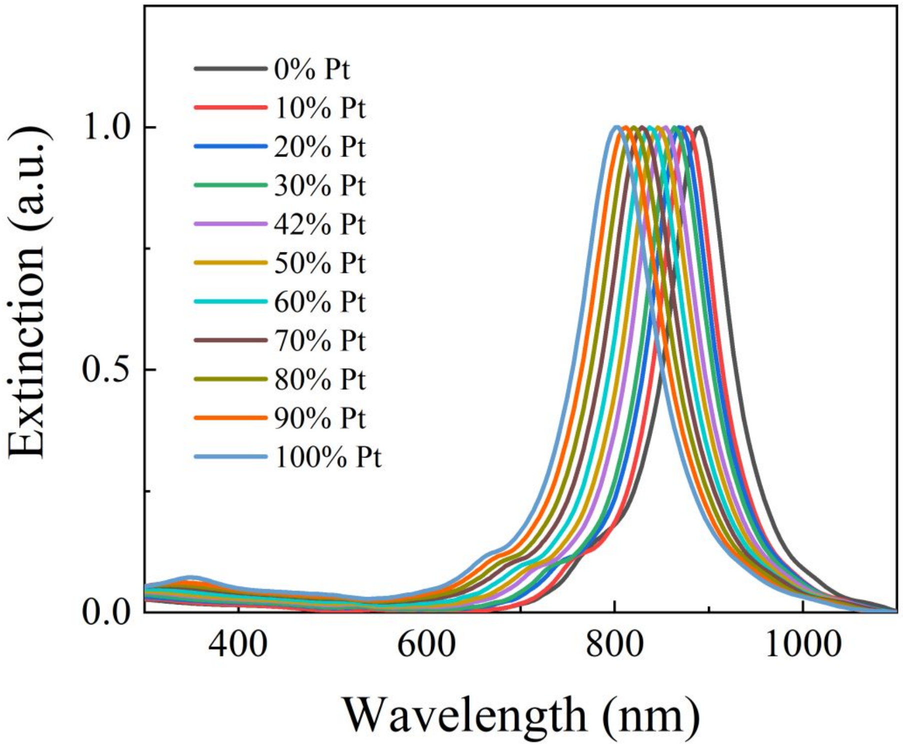

Figure S22. FDTD simulations of the extinction spectra with different Ag-to-Pt ratios of AgPt alloy in a single Au@AgPt HAS. When the ratio of Pt increasing in AgPt alloy, the LSPRs blue-shifted. All the AgPt alloy shell are 4 nm in simulation.

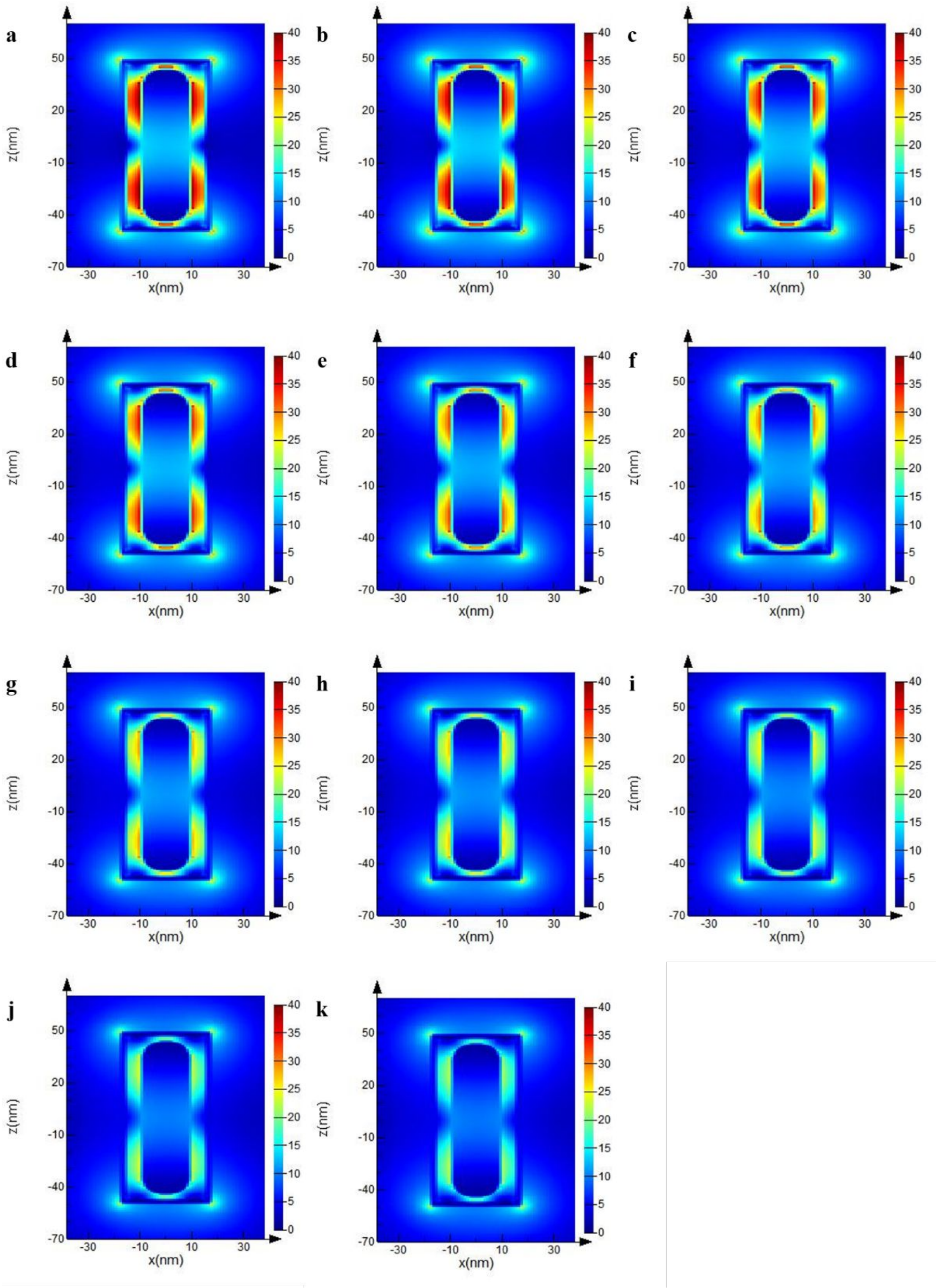

Figure S23. FDTD simulations of electric field distributions with different ratios of Ag-to-Pt (a) 1, (b) 9:1, (c) 8:2, (d) 7:3, (e) 6:4, (f) 5:5, (g) 4:6, (h) 3:7, (i) 2:8, (j) 1:9, (k) 0 of AgPt alloy in a single Au@AgPt HAS. When the ratio of Pt increasing in AgPt alloy, the electric field enhancement decreased. All the AgPt alloy shell are 4 nm.

Table S1 the parameters of Au@AgPt with different amount of reactants.

samples	$AgNO_3$ (mL)	K_2PtCl_4 (mL)	LSPR (nm)
AuNRs	0.20	0	882
Au@Ag	0.20	0	692
Au@Pt	0	0.04	883
Au@AgPt heterostructure	0.01	0.04	982
Au@AgPt	0.02	0.04	992
Au@AgPt	0.04	0.04	988
Au@AgPt	0.06	0.04	945
Au@AgPt	0.08	0.04	911
Au@AgPt	0.10	0.04	898
Au@AgPt	0.15	0.04	844
Au@AgPt HAS	0.20	0.04	815
Au@AgPt	0.25	0.04	795
Au@AgPt	0.30	0.04	667
Au@AgPt	0.35	0.04	677
Au@AgPt	0.40	0.04	729
Au@AgPt	0.10	0.04	827
Au@AgPt	0.10	0.04	908
Au@AgPt	0.10	0.08	900
Au@AgPt	0.10	0.10	970
Au@AgPt	0.10	0.15	1015
Au@AgPt dendritic	0.10	0.20	/
Au@AgPt dendritic	0.10	0.25	/
Au@AgPt dendritic	0.10	0.30	/
Au@AgPt dendritic	0.10	0.35	/
Au@AgPt dendritic	0.10	0.40	/

Table S2 Pearson's coefficient of the reaction rate under light illumination in Figure 3d, g.

condition	samples	Pearson's coefficient
light	0.01 mL $AgNO_3$, 0.04 mL K_2PtCl_4	0.99
light	0.08 mL $AgNO_3$, 0.04 mL K_2PtCl_4	0.99
light	0.15 mL $AgNO_3$, 0.04 mL K_2PtCl_4	0.99
light	0.20 mL $AgNO_3$, 0.04 mL K_2PtCl_4	1
light	0.30 mL $AgNO_3$, 0.04 mL K_2PtCl_4	0.96
light	0.10 mL $AgNO_3$, 0.04 mL K_2PtCl_4	0.99
light	0.10 mL $AgNO_3$, 0.10 mL K_2PtCl_4	0.98
light	0.10 mL $AgNO_3$, 0.20 mL K_2PtCl_4	0.98

Table S3 Pearson's coefficient of the reaction rate under dark condition in Figure 3d,g.

condition	samples	Pearson's coefficient
dark	0.01 mL $AgNO_3$, 0.04 mL K_2PtCl_4	0.99
dark	0.08 mL $AgNO_3$, 0.04 mL K_2PtCl_4	0.98
dark	0.15 mL $AgNO_3$, 0.04 mL K_2PtCl_4	0.99
dark	0.20 mL $AgNO_3$, 0.04 mL K_2PtCl_4	0.97
dark	0.30 mL $AgNO_3$, 0.04 mL K_2PtCl_4	0.99
dark	0.10 mL $AgNO_3$, 0.04 mL K_2PtCl_4	0.97
dark	0.10 mL $AgNO_3$, 0.10 mL K_2PtCl_4	0.92
dark	0.10 mL $AgNO_3$, 0.20 mL K_2PtCl_4	0.93